Effects of residue substitutions on the cellular abundance of proteins

Thea K. Schulze[1] **and Kresten Lindorff-Larsen**[1*]

***For correspondence:** lindorff@bio.ku.dk (K.L.-L.)

[1]The Linderstøm-Lang Centre for Protein Science, Department of Biology, University of Copenhagen, Ole Maaløes Vej 5, DK-2200 Copenhagen, Denmark

Abstract

Multiplexed assays of variant effects (MAVEs) make it possible to measure the functional impact of all possible single amino acid residue substitutions in a protein in a single experiment. Combination of variant effect data from several such experiments provides the opportunity to conduct large-scale analyses of variant effect scores measured across proteins, but can be complicated by variations in the phenotypes that are probed across experiments. Thus, using variant effect datasets obtained with similar MAVE techniques can help reveal general rules governing the effects of amino acid variation for a single molecular phenotype. In this work, we accordingly combined data from six individual variant abundance by massively parallel sequencing (VAMP-seq) experiments and analysed a total of 31,614 variant effect scores reporting solely on the impact of single amino acid residue substitutions on the cellular abundance of proteins. Using our combined variant effect dataset, we derived and analysed a collection of amino acid substitution matrices describing the average impact on cellular abundance of all residue substitution types in different structural environments. We found that the substitution matrices predict the cellular abundance of protein variants with surprisingly high accuracy when given structural information only in the form of whether a residue is buried or exposed. We thus propose our substitution matrix-based predictions as strong baselines for future abundance model development.

Introduction

The twenty commonly occurring amino acids have vastly different physicochemical properties, which allow them to play distinct roles for protein structure formation and function. Some amino acid residues might be particularly important for the thermodynamic and cellular stability of a certain protein and others crucial for intrinsic activity or function, with the different amino acid residue types contributing to each of these properties in unique ways (***Ribeiro et al., 2020***; ***Dunham and Beltrao, 2021***; ***Tsuboyama et al., 2023***; ***Cagiada et al., 2024***). For certain aspects of protein functionality, the role played by each type of amino acid to maintain this functionality is well-understood. For example, the propensity of each of the twenty amino acids to form or break secondary structural elements has been studied extensively. The typical way to assess the role played by different amino acids in proteins is by using mutagenesis studies. The experimental methods available for performing such studies have developed immensely, and the field has thus progressed from investigating single or few residue substitutions at a time, to conducting alanine scans, to now using saturation mutagenesis methods, including MAVEs, that allow the impact of thousands of residue substitutions on protein structure and function to be studied in a single experiment (***Fowler and Fields, 2014***).

The wealth of mutagenesis data collected in for example MAVE experiments can be used to

analyse substitution effects in individual proteins comprehensively. The data moreover provides the opportunity to conduct large-scale studies to uncover general rules regarding the properties and functions of amino acid residue types across proteins, if data reporting on substitution effects in multiple proteins is combined. Some MAVEs assess the effects of residue substitutions on several proteins in a single experiment (***Rocklin et al., 2017***; ***Tsuboyama et al., 2023***; ***Beltran et al., 2024***), thus naturally allowing the latter type of analysis. However, most studies investigate substitution effects in a single protein at a time, and metaanalysis thus requires that data from different individual experiments are combined (***Gray et al., 2017***; ***Dunham and Beltrao, 2021***; ***Høie et al., 2022***). Such metaanalyses have proven very useful and have, among other things, revealed 100 amino acid subtypes based on substitution effect profiles (***Dunham and Beltrao, 2021***) and provided insight into which amino acid types that best discriminate protein-ligand binding interface from non-interface residues across proteins (***Gray et al., 2017***).

While combining substitution effect scores from several MAVEs allows for creation of large datasets, such an approach must take into consideration that the term MAVE covers a range of experimental methods that seek to investigate different aspects of protein function and use a variety of techniques for this purpose (***Weile and Roth, 2018***; ***Tabet et al., 2022***; ***Geck et al., 2022***). MAVE methods share a common foundation, namely setting up a system linking protein sequence or genotype to a phenotypic readout that can be selected for on large scale and traced back to genotype via sequencing (***Fowler and Fields, 2014***; ***Fowler et al., 2014***). However, the molecular phenotype being studied and the selection mechanism used change from assay to assay. Some studies might take interest in variant effects on enzymatic activity or ligand binding affinity, while others might be concerned with the impact of substitutions on cellular fitness, to give a few examples. Ultimately, these assays are thus expected to report on overlapping, but non-identical variant effects. MAVEs are additionally performed in various experimental backgrounds, for instance in different organisms and at different temperatures, which influence measured variant effect scores. It has been demonstrated that changing a single parameter related to the experimental background, for example expression level (***Jiang et al., 2013***; ***Cisneros et al., 2023***) or the chemical (***Mavor et al., 2016***, ***2018***; ***Weile et al., 2021***) or genetic (***Thompson et al., 2020***; ***Nguyen et al., 2024***) background, can result in substantial differences to the MAVE readout. In an aggregated dataset consisting of a variety of MAVE scores, phenotype- or background-specific effects will thus likely be present and add noise to the analysis performed with the dataset. A final obstacle for MAVE score combination is that the effects of substitutions are quantified in different ways across experiments (***Peterman and Levine, 2016***; ***Rubin et al., 2017***), meaning that score combination typically requires implementation of one (***Gray et al., 2017***; ***Munro and Singh, 2021***; ***Høie et al., 2022***) or several (***Dunham and Beltrao, 2021***) score transformation schemes to make scores from individual datasets compatible (or at least be on the same scale).

As the number of published MAVE datasets has grown (***Esposito et al., 2019***; ***Rubin et al., 2021***), it has become increasingly feasible to perform metaanalysis of combined datasets that were obtained with similar methodologies and report on the same molecular phenotypes. On this basis, it is possible not only to decrease potential background noise, but also to discover general rules governing residue substitution effects for that specific phenotype. Thus, inspired by several previous MAVE data-based, large-scale analyses of substitution effects (***Gray et al., 2017***; ***Dunham and Beltrao, 2021***) and the recent availability of homogeneous MAVE data, we here analysed a collection of six MAVE datasets that all report on the impact of single residue substitutions on protein cellular abundance. Our analysis is thus focused on a single molecular phenotype, cellular abundance, which is known to be crucial for protein function and at the same time easily impacted by substitution of single residues, with widespread consequences for human disease (***Matreyek et al., 2018***; ***Cagiada et al., 2024***).

Variant cellular abundance has been studied with different MAVE setups, including through protein fragment complementation assays that rely on monitoring cell growth (***Faure et al., 2022***) and by using fluorescent reporters to estimate cellular concentration (***Matreyek et al., 2018***). The

substitution effects analysed here were all measured using the same type of MAVE experiment, specifically VAMP-seq, and the analysed effects were thus all observed in highly similar experimental backgrounds and were quantified with the same selection mechanism using almost identical methods (***Matreyek et al., 2018***, ***2021***; ***Amorosi et al., 2021***; ***Suiter et al., 2020***; ***Grønbæk-Thygesen et al., 2024***; ***Clausen et al., 2024***). The VAMP-seq method estimates the steady-state abundance of all single residue substitution variants of a protein through expression of green fluorescent protein-tagged protein variants in cultured human cells. Each cell expresses a single protein variant, and the cellular fluorescence intensity thus reports on the cellular abundance of the expressed variant. Abundance scores for thousands of variants are obtained in high-throughput by separating cells into bins of discrete fluorescence intensity intervals using fluorescence-activated cell sorting (FACS) followed by sequencing of each bin. Expression is controlled for, and changes in abundance are therefore mostly a product of changed degradation behaviour due to the substitution of residues (***Matreyek et al., 2018***).

The six VAMP-seq datasets have all been analysed extensively, and separately, in previous work (***Matreyek et al., 2018***, ***2021***; ***Amorosi et al., 2021***; ***Suiter et al., 2020***; ***Cagiada et al., 2021***; ***Grønbæk-Thygesen et al., 2024***; ***Clausen et al., 2024***). Here, we combined the six datasets and thereby obtained a total of 31,614 abundance variant effects scores, allowing us to perform a large-scale analysis of the impact of single residue substitutions on cellular abundance across proteins and thus contribute to our understanding of how different amino acid residues help maintain cellular protein levels. In our analysis, we specifically focused on analysing and predicting the impact of residue substitutions on abundance using only simple considerations of the structural environment of residues. Simple structural descriptors, such as local packing density and the difference in side-chain accessible surface area burial upon folding between wild-type and variant residues, have previously been shown to capture some substitution effects on protein folding stability, for example for cavity-creating substitutions (***Serrano et al., 1992***; ***Chakravarty and Varadarajan, 1999***; ***Cota et al., 2000***). The impact of substitutions on protein stability can to some extent also be predicted when a simple structural descriptor like residue relative solvent accessibility is used in combination with information about the physicochemical properties of wild-type and variant residues (***Caldararu et al., 2021***). Since substitutions that affect the free energy of folding of a protein tend to also have an impact on cellular abundance (***Nielsen et al., 2017***; ***Scheller et al., 2019***; ***Abildgaard et al., 2019***; ***Matreyek et al., 2018***; ***Suiter et al., 2020***; ***Cagiada et al., 2021***; ***Høie et al., 2022***; ***Gerasimavicius et al., 2023***; ***Grønbæk-Thygesen et al., 2024***; ***Clausen et al., 2024***), similar structural descriptors might also be useful for analysis of cellular stability substitution effects. Our goal in this work is ultimately thus not to develop the most accurate possible variant abundance predictor, but rather to show how much variation in cellular abundance can be understood by simple rules that apply across different proteins.

For our structure-based analysis of the combined VAMP-seq dataset, we constructed a set of amino acid substitution matrices that for different structural environments contain the average abundance scores for all possible residue substitution types. Others have in earlier work similarly calculated substitution matrices using experimental mutagenesis data and studied the ability of the matrices to predict the impact of mutations (***Yampolsky and Stoltzfus, 2005***; ***Munro and Singh, 2021***; ***Høie et al., 2022***). The matrices presented here are, however, both cellular abundance- and structure context-specific. We provide an extensive analysis of the constructed matrices and use the matrices to show that a considerable amount of the variation in the VAMP-seq data can be explained by taking only residue solvent accessibility in the structure of the wild-type proteins into account together with wild type and variant residue types. Our results thereby highlight that simple biochemical considerations can compete with complex biophysics-based models for predicting the impact of residue substitutions on cellular abundance, although we note that predictions are in both cases non-perfect and that more work is needed before the abundance of protein variants can be accurately modelled. Finally, we also use the substitution matrices to propose a simple approach that, given a saturation mutagenesis dataset for the protein of interest, can be used to

assess structural models of the protein under the *in vivo* conditions used for the MAVE.

Results and Discussion

Overview of VAMP-seq datasets

To perform our large-scale analysis of residue substitution effects on protein cellular abundance, we first collected previously published VAMP-seq data for six soluble human proteins, all known to be involved in human disease or drug metabolism. Although VAMP-seq has been applied to membrane proteins (***Chiasson et al., 2020***; ***Amorosi et al., 2021***), residue substitutions might affect the cellular abundance of membrane and non-membrane proteins at least partially through different mechanisms (***Chiasson et al., 2020***), and we therefore limited our study to only include soluble proteins. Our dataset thus consisted of PTEN (***Matreyek et al., 2018***, ***2021***), TPMT (***Matreyek et al., 2018***), CYP2C9 (***Amorosi et al., 2021***), NUDT15 (***Suiter et al., 2020***), ASPA (***Grønbæk-Thygesen et al., 2024***) and PRKN (***Clausen et al., 2024***) VAMP-seq scores (Table S1). We realise that CYP2C9 is in fact anchored to the endoplasmic reticulum membrane through an N-terminal, transmembrane helix, but the protein consists mostly of a large domain found in the cytoplasm (***Amorosi et al., 2021***), and we therefore included abundance scores for residues found in the cytoplasmic, soluble domain in our analysis.

The variant abundance scores for each of the proteins in our dataset were measured in individual VAMP-seq experiments, and the six experiments were all performed by sorting variant-expressing cells into four equally populated bins based on cellular fluorescence intensities. In all cases, the cellular abundance of a variant was quantified by taking a weighted average of the variant frequency across the four bins. The resulting scores were for each protein normalised so that a variant abundance score of 0 corresponds to nonsense-variant-like abundance and of 1 to wild-type-like abundance. We summarised and compared the six datasets by calculating a number of dataset descriptors and by mapping average abundance scores per position onto the protein structures (Fig. 1). When combined, the six VAMP-seq datasets contain in total 31,614 single residue substitution variant abundance scores. The scores span the full lengths of the protein sequences, although the mutational depth, that is, the average number of substitutions per residue position with a reported score after quality filtering, varies considerably from protein to protein (Fig. 1B). The mutational completeness of the datasets vary accordingly, with a minimum of 57% for PTEN and a maximum of 99% for PRKN (Fig. 1C). As the proteins also have different sequence lengths (Table S1), they contribute unequally to the total pool of variants (Fig. 1D).

We note that in spite of the similar experimental methodology and strategy for calculation of reported scores there are considerable differences between the shapes of the abundance score distributions obtained in the six experiments (Fig. S1). PTEN, TPMT and CYP2C9 have abundance score distributions with broad peaks at low and high abundance, whereas NUDT15, ASPA and PRKN have almost binary distributions with narrow peaks, in particular for abundance scores close to 0. All distributions appear bimodal, with the exception of the CYP2C9 score distribution, which has an additional peak around 0.5. Low abundance scores are generally distributed around 0, but for PTEN, the low abundance-peak is shifted towards higher scores. The reported abundance score standard deviations also differ in magnitude across datasets (Fig. S2). To represent the noise level in each dataset using a single number, we resampled the individual score distributions based on score standard deviations and calculated Pearson's correlation coefficient, r, between the original datasets and the resampled datasets. In addition to indicating the dataset noise levels, the resulting r values also provide an upper bound for how well abundance score predictions from a perfect variant abundance model would correlate with the experimental data (Fig. 1E). Since dataset noise levels and the broadness of peaks in score distributions appear correlated, we assume that the distribution shape differences originate at least partly from the varying noise levels in the datasets. However, since an equal number of cells was sorted into each of the four bins during the FACS-step of the VAMP-seq experiments, across-experiment differences in the compositions of sorted

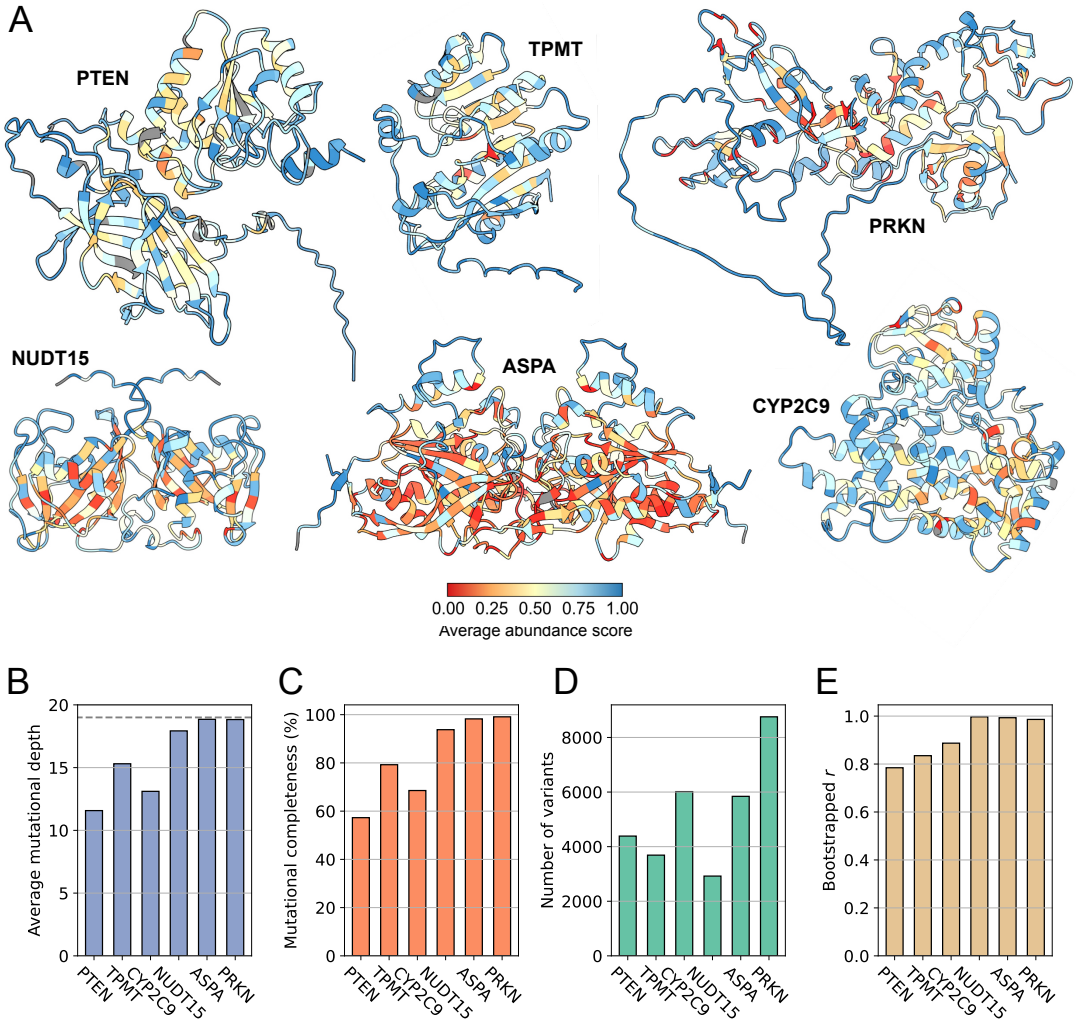

Figure 1. Overview of VAMP-seq datasets and proteins. (A) Structures of proteins previously studied with VAMP-seq coloured by average VAMP-seq abundance score per residue. Averages are shown for all residues with abundance scores available, even if only one or few scores have been reported for the residue. Homodimer structures are shown for NUDT15 and ASPA, and residues with no reported scores are shown in gray. (B–E) Overview of VAMP-seq dataset sizes, completenesses and noise levels, showing specifically (B) the average number of variant scores per residue position, with 19 (indicated with dashed line) being the highest possible value, (C) mutational completeness, that is, the percentage of all possible single residue substitution variants with an abundance score in the dataset, (D) the total number of single residue substitution abundance scores per protein, and (E) Pearson's correlation coefficient r between originally reported and resampled abundance score datasets, with resampling based on reported abundance score standard deviations.

cell libraries likely also contribute to the described distribution differences. Finally, we note that the distribition differences to some extent possibly also reflect dissimilar wild type protein melting temperatures, as previously suggested for PTEN and TPMT (***Matreyek et al., 2018***).

Abundance score predictions from simple structural considerations

Our mapping of the average abundance score per residue onto the protein structures shows expected and previously described trends, most obviously that many solvent-exposed residues have high average abundance scores and that substitutions of core residues decrease abundance on average (Fig. 1A). Exceptions to these patterns exist, as some solvent-exposed residues for instance appear intolerant to substitution. These exceptions have to some extent been described and analysed in the original VAMP-seq publications. We note that the average abundance scores differ in magnitude from protein to protein, in particular in core regions.

To quantify the relation between the structural context and mutational tolerance of a residue in the context of abundance, we used the wild-type structures of the six proteins, which have relatively similar structural compositions (Fig. S3), to calculate features describing local residue environment, including relative solvent accessible surface area (rASA) and weighted contact number (WCN). The WCN of a residue quantifies contact formation with all other residues in the protein so that a residue in a densely packed region will have a high WCN and vice versa. While rASA is sensitive to different residue environments on or close to the protein surface, rASA does not capture variation in the structure within the protein core. On the contrary, WCN has dynamic range for buried residues and is thus a complementary descriptor. Both rASA and WCN correlate moderately well with the abundance scores, although the correlations are considerably higher for some proteins (PRKN and TPMT) than others (ASPA) (Fig. S4, S5). Generally, rASA captures the ranking of variant effects better than the WCN; Spearman's rank correlation coefficient, r_s, is on average 0.45 (0.54) between abundance scores and rASA and 0.41 (0.43) between abundance scores and WCN when including all datasets (or when including all except for ASPA) (Fig. S4). When looking at the average abundance score per residue, we found solvent-exposed residues with reduced to strongly reduced abundance in all proteins, though in particular in ASPA and PRKN. Some residues buried in the structures on the other hand appear mutationally tolerant (Fig. S5).

Given the correlations between abundance scores and rASA and WCN described in the above, we hypothesised that combining the simple structural descriptors with information about the physicochemical properties of the wild type and variant amino acid residue types would allow us to explain the effects of many substitutions on cellular abundance. To test this hypothesis, we first established a baseline framework without using structural information, after which we extended our analysis to take structure into account. For the structure-free analysis, we used the combined pool of abundance scores from all six proteins to construct a substitution matrix that, for each of the 380 possible amino acid residue substitution types, contains the abundance score average (Fig. S7). We tested the ability of the substitution matrix to act as an abundance score predictor using leave-one-protein-out cross-validation; that is, we recalculated the matrix leaving out the entire VAMP-seq dataset from a single protein and then used the averages in the recalculated matrix as abundance score predictions for substitutions in the omitted protein. While the average abundance scores are not particularly good predictors of variant abundance (Fig. 2C, S8), some signal in the experimental data is indeed captured even without considering the structural context of the wild-type residues (Fig. S8). Previous studies have reached similar conclusions in analyses that calculate structure-independent substitution matrices and predict variant fitness by combining data from a variety of MAVE experiments (***Munro and Singh, 2021***; ***Høie et al., 2022***).

We next explored whether we could improve upon this baseline by taking simple structural features into account. We used rASA values calculated for the wild-type protein structures to classify all residues as either solvent-exposed or structurally buried (Fig. S6). We then calculated two new substitution matrices, in one matrix averaging over variant abundance scores from residues belonging to the solvent-exposed class and in the other over scores from buried residues. Using the same

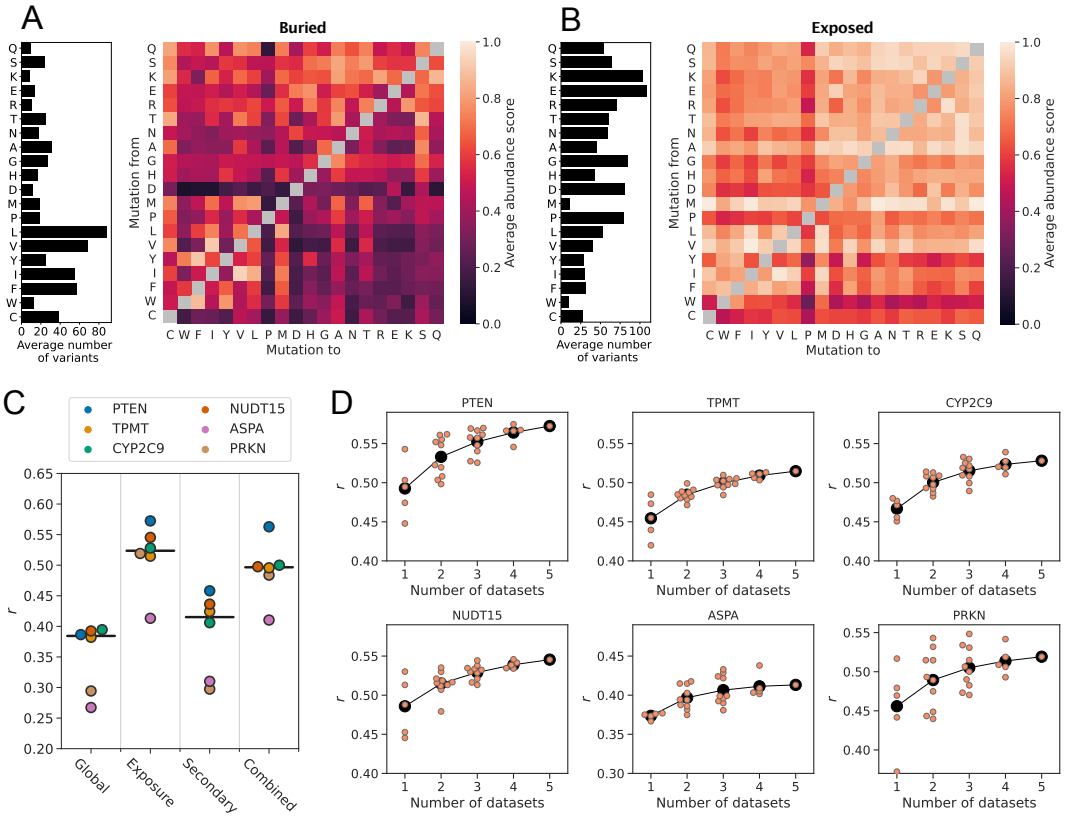

Figure 2. Average abundance score substitution matrices predict unseen abundance data. Average abundance scores for all possible amino acid residue substitution types for residues sitting in either (A) structurally buried or (B) solvent-exposed environments in the wild-type protein structures. The bar plot to the left of each substitution matrix indicates the average number of abundance scores that was used to calculate score averages in each row of the matrix. Amino acids are sorted according to row averages in the global substitution matrix (Fig. S7). (C) Correlations between experimental abundance scores and abundance scores predicted from average abundance score substitution matrices using leave-out-one-protein cross-validation. The matrices used for predictions were constructed using all data (Global) and for different residue categories based on residue solvent-exposure (Exposure), secondary structure (Secondary) or both solvent-exposure and secondary structure (Combined). The vertical black bars mark the median correlation coefficient for each category. (D) Correlations between experimental abundance scores and abundance scores predicted from average abundance score substitution matrices for residues sitting in either buried or exposed environments. Scores were predicted for each protein (indicated above each plot) using average abundance score substitution matrices calculated using an increasing number of VAMP-seq datasets. Orange data points mark the prediction result from a single specific combination of datasets, and the average for each dataset count is indicated with black circles.

approach as above, we evaluated how well our exposure-based substitution matrices could predict unseen abundance data using leave-one-protein-out cross-validation. The abundance score prediction of a variant was thus obtained by looking up the abundance score average of the relevant substitution type in either the exposed or buried residue matrix depending on the structural class of the residue for which a prediction was made. Accounting for the structural context of the wild-type residue considerably increases the ability of the model to capture the impact of substitutions on abundance, with the median r across datasets increasing from 0.39 to 0.53 when not only the substitution type but also the degree of residue solvent-exposure is considered (Fig. 2C). While combining simple structural features with information about the wild-type and variant residue types hence allows us to explain the effects of many substitutions on the cellular abundance of a protein, it is at the same time clear that the consequences of some substitutions are not properly captured within this framework. We in particular find one group of common outliers in predictions of the NUDT15, ASPA and PRKN datasets, namely substitutions that experimentally have strongly reduced abundance scores, but which the exposure-based substitution matrix models predict to have wild-type-like or nearly wild-type-like abundance (Fig. S9).

We tested if additional substitution effects could be captured by also considering the secondary structure context of residues in the wild-type structures. To perform this analysis, we calculated two new sets of substitution matrices. In the first set, we averaged abundance scores for residues in different types of secondary structure and thereby obtained three matrices containing average effects in helix, stand and loop structure (Fig. S7). To create the other set of matrices, we split residues by both secondary structural class and degree of solvent-exposure, creating residue classes such as "solvent-exposed helix" and "structurally buried strand", which resulted in six matrices of average effects. We performed abundance score predictions with the two sets of matrices using the cross-validation approach described in the above. The substitution matrix set based only on residue secondary structure context performs only slightly better in the prediction task than the structure-independent matrix, although the performance difference depends on the protein for which predictions are made (Fig. 2, S10), and secondary structure is by itself thus not a suited descriptor for capturing abundance variant effects. The combination of solvent-exposure-degree and secondary structure class similarly does not improve predictions compared to when only exposure-degree is used (Fig. 2, S11).

Since our VAMP-seq dataset is relatively small and limited to six proteins, we next assessed if our substitution matrix-based abundance models could be expected to improve with the addition of more VAMP-seq data in the future. For this assessment, we recalculated all exposure-based matrices using all possible combinations of the six datasets. We then performed predictions again, for every protein using all matrices in which the data for this protein did not occur to perform predictions. In this way, we estimated how r varied with the number of datasets included in the substitution matrix calculation. While using more datasets improves predictions on average, we observe that, depending on the exact combination of datasets, predictions can be as good or better when only one or few datasets are used to obtain the abundance score averages as when five datasets are used (Fig. 2D). Some datasets thus appear to be more related than others, which might be due to either (*i*) the dataset similarities and differences described under *Overview of VAMP-seq datasets* or (*ii*) some proteins potentially having a larger overlap between the environments that their residues are sitting in than others (Fig. S17). The average r seems for each protein to be plateauing or have only a small slope, suggesting that this framework would likely only improve to a small degree with the addition of more data in the future. We observed similar trends when we performed the same analysis for the Combined matrices (Fig. S15).

To provide context for the numbers reported in the above, we compared abundance score prediction results obtained with our substitution matrices to predictions based on calculation of the thermodynamic stability change, $\Delta\Delta G$, caused by residue substitution. We and others have previously observed a correlation between variant cellular abundance and $\Delta\Delta G$, both in low-throughput cellular studies (***Nielsen et al., 2017***; ***Scheller et al., 2019***; ***Abildgaard et al., 2019***) and in high-

throughput VAMP-seq studies (***Matreyek et al., 2018***; ***Suiter et al., 2020***; ***Cagiada et al., 2021***; ***Høie et al., 2022***; ***Gerasimavicius et al., 2023***; ***Grønbæk-Thygesen et al., 2024***; ***Clausen et al., 2024***), and we thus consider ΔΔG calculations to be a baseline abundance model with a mechanistic basis. As observed in previous work, we find that variant ΔΔG values estimated with the Rosetta energy function (***Park et al., 2016***) correlate with VAMP-seq abundance scores (Fig. S12). While this is the case for all six proteins in our dataset, there are noticeable differences in the magnitude of the rank correlation coefficient across datasets; r_s ranges from -0.45 for PRKN to -0.59 for NUDT15. The rank correlation coefficients between experimental and predicted abundance scores are similar for predictions obtained with the Rosetta energy function and with the exposure-based substitution matrices for four out of six proteins in our dataset (Fig. S9, S12). As abundance score predictor, our method based on exposure-based substitution matrices of average abundance scores is thus competitive with Rosetta, in spite of the complexity of the energy function and the post-mutation structural sampling performed as part of the ΔΔG calculation pipeline. We thus propose our matrix-based predictions as a strong baseline for future abundance model development.

Analysis of abundance score substitution matrices

We find that the average substitution effects are in general in accordance with biochemically expected and previously observed patterns (***Munro and Singh, 2021***; ***Høie et al., 2022***). Across residue environments, substitutions conserving the physicochemical properties of the reference residue are often tolerated well, or at least better than non-conservative substitutions, and it is moreover clear that residues found in structurally buried environments tolerate substitutions less than solvent-exposed residues (Fig. 2A,B). While substitution of residues in buried environments likely decrease protein cellular abundance on average because the thermodynamic stability is compromised, substitution of exposed residues might affect cellular stability through different mechanisms (***Marrero and Barrio-Hernandez, 2021***), for instance by interference with formation of intermolecular interactions (and thus potentially thermodynamic stability of complexes) (***Suiter et al., 2020***; ***Grønbæk-Thygesen et al., 2024***) or through modification of exposed degradation motifs (***Clausen et al., 2024***). We observe that, at solvent-exposed sites, substitutions from polar or charged residues to non-polar or aromatic residues are not tolerated as well as conservative substitutions. Comparing matrices across residue environments shows that substitution to proline is, as expected and previously observed, not tolerated well in any environment, and substitution from proline is also often disruptive. Mutation of cysteine to any other residue also appear to reduce abundance considerably on average in several environments. However, leaving out PRKN abundance scores from the calculation of the averages makes mutation from cysteine much less disruptive (Fig. S13), and the average effects when all proteins are included are thus dominated by the Zn^{2+}-coordinating cysteine residues that are critical for the abundance of PRKN (***Clausen et al., 2024***).

In line with expectations and previous results (***Munro and Singh, 2021***; ***Høie et al., 2022***), the global, structure-independent matrix is furthermore asymmetric (Fig. S7), that is, for many residue pairs, substitution from residue *X* to *Y* tend to affect abundance differently than substitution from residue *Y* to *X*. In the global context, substitutions from non-polar or aromatic residues to polar or charged residues for example tend to be more disruptive than the opposite substitutions. Such asymmetry is, per construction, not present in traditional substitution matrices used for construction of sequence alignments (***Dayhoff et al., 1978***; ***Henikoff and Henikoff, 1992***), although more recent work has derived asymmetric matrices using sequence data (***Dang et al., 2022***). The matrix with average abundance scores from buried residues is also asymmetric, in spite of the fact that substitutions from polar or charged residues to hydrophobic or aromatic residues (and not only the opposite) tend to be quite disruptive of abundance in buried environments (Fig. S7). While some asymmetric features are still present when only solvent-exposed residues are considered, the asymmetry is less pronounced, meaning that non-conservative substitutions often affect cellular stability relatively similarly irrespective of the biochemistry of the wild-type residue in this

structural environment (Fig. S7).

From visual inspection of the substitution matrices, it is clear that certain pairs and groups of amino acid types share a number of substitution profile features. In a given environment, each amino acid type has two substitution profiles in form of the two vectors of nineteen abundance score averages describing effects of substitution to or from the given amino acid. We explored substitution profile similarities by performing hierarchical clustering of the average score matrices, focusing our analysis on effects in buried and exposed environments (Fig. 3A). The analysis of buried residues identifies several clusters that are in accordance with residue biochemistry; for example, when considering mutational profiles for substitutions *to* a given residue, one cluster contains the aromatic residues, another cluster consists of several non-polar residues, and residues with similar charges are identified as closely related. We moreover observed that, in buried environments, substitutions to glycine are in many cases as detrimental as substitutions to polar or charged residues. The clustering also highlights that substitutions from non-polar residues to the aromatic residues are not well-tolerated on average, potentially due to differences in the volume of the side chain. In fact, substitutions from non-polar buried residues to the aromatic residues share features with substitutions from non-polar buried residues to charged or polar residues. In the exposed environment, we also found clusters that are generally in accordance with residue biochemistry.

For both structurally buried and solvent-exposed environments, several residue groups identified in the clustering of the matrix rows are also are also identified in the clustering of the matrix columns. However, the dendrograms along the two axes are not identical, neither in the buried nor in the exposed context. The order in which clusters form depend on the axis, and some residues appear in different clusters depending on whether they are being mutated from or to. For example, serine cluster with the majority of polar and charged residues in the *mutation from* direction in the buried matrix, but not in the *mutation to* direction. More surprisingly, aspartate and glutamate behave similarly when they occur as the variant residue in the buried environment, but have more different mutational patterns when they are the wild type residue. Generally, buried aspartate appears to play a critical role for maintaining abundance and is clearly an outlier in the *mutation from* direction, as it does not seem to cluster with any other residues. Even mutation from aspartate to glutamate is not tolerated well in the protein core, highlighting that the importance of buried aspartate for cellular stability is not only charge-related. In the exposed environment, aspartate and glutamate do cluster together as both wild-type and variant residues. However, tryptophan, tyrosine and cysteine appear more distantly related to the non-polar and aromatic residues in mutation from than in mutation to direction in this environment.

We further quantified the relations between the substitution profiles of the 20 amino acids using principal component analysis (PCA). As input for this analysis, we reformatted our substitution matrices so that they for each of the 20 amino acid residue types contained a 40-vector consisting of the 20 *mutation to* and 20 *mutation from* abundance score averages for that residue type. In that way, the PCA explored amino acid similarities and differences considering simultaneously the effects of substitution from and to a given amino acid. For buried residues, the first principal component (PC1) appears to separate the polar and charged amino acids from the nonpolar and aromatic amino acids (Fig. 3B), showing (as expected) that amino acid hydrophobicity is an important property for explaining variation in the substitution profiles in buried environments. Along PC1, proline and glycine are placed close to the group consisting of polar and charged amino acids. PC2 for buried residues clearly separates the nonpolar/aliphatic and aromatic residues, and along the PC2 axis, most polar residues are found at a shorter distance to the nonpolar residues than the aromatics, indicating a closer relationship with the former group. The PCA of average abundance scores in exposed environments separates the nonpolar and aromatic amino acids from the remaining amino acids along PC2 rather than PC1. The PC1 for residues in an exposed environment, which on its own explains a relatively high amount of variation in the substitution profiles, instead seems at least partially correlated with how well substitutions to polar and charged residues are

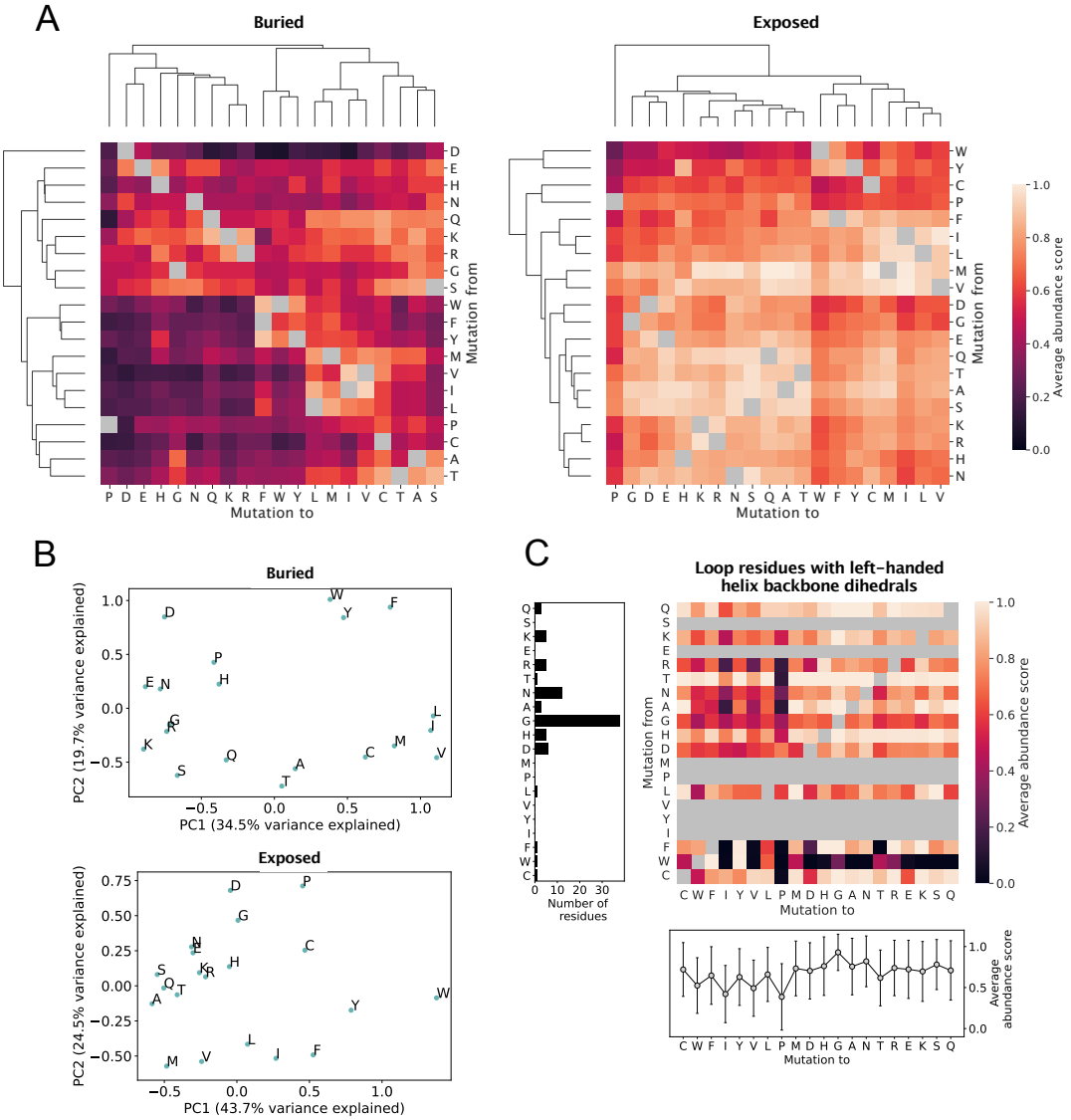

Figure 3. Analysis of average abundance score substitution matrices. (A) Hierarchical clustering of average abundance score substitution matrices for buried and solvent-exposed environments. Clustering was performed along both axes of the matrices. Grey squares indicate a synonymous substitution. (B) Principal component analysis of substitution profiles describing the effects of all substitutions from and to each of the twenty amino acid residues. The analysis was performed using average abundance scores for residues in buried and exposed environments separately. (C) Analysis of substitution profiles of loop residues with backbone dihedral angles similar to those found in left-handed helices. The heat map shows average abundance scores for all loop residues with left-handed helix-like backbone dihedral angles in the six proteins. Grey squares indicate a synonymous substitution as well as no data. The plot below the heat map shows average abundance scores for substitutions to each of the twenty amino acid residues for this particular class of loop residues, with error bars indicating the standard deviation over all abundance scores for the substitution type. The left bar plot shows the total number of loop residues that for each residue type was found across the six proteins to adopt the left-handed helix-like backbone conformation.

tolerated (Fig. 3B).

Given the correlation between stability and abundance described in the above (Fig. S12), we hypothesised that we might find residue substitution patterns known to be associated with protein thermodynamic stability in the average abundance score substitution matrices. We therefore tested the correlation between average abundance scores for residues found in α-helices and different experimentally and statistically derived residue helix propensity scales (***Pace and Scholtz, 1998***). All correlations between average abundance scores and helix propensity scales are weak (Fig. S16), indicating that the average abundance substitution patterns are not dominated by helix propensities. A similar observation was made in a study aggregating data from a broader range of MAVEs (***Gray et al., 2017***).

For residues in loops, we noticed that glycine, histidine, asparagine and aspartate share certain substitution profile features, as they all appear particularly sensitive to mutation to β-branched residues, including threonine, isoleucine and valine, as well as to tryptophan and proline (Fig. S7). In loop structure, many residues, and in particular exactly glycine, histidine, asparagine and aspartate, are able to adopt backbone ϕ and ψ angles in the $0^\circ < \phi < 180^\circ$, $-90^\circ < \psi < 90^\circ$ area of the Ramachandran plot (***Hovmöller et al., 2002***). Backbone dihedral angles in this region of the Ramachandran plot are associated with left-handed helix formation, although the vast majority of residues adopting these dihedral angles do not actually take part in forming left-handed helix (***Hovmöller et al., 2002***). A number of residue types, including isoleucine, threonine, proline and valine, have very little density in this region of the Ramachandran plot (***Hovmöller et al., 2002***). We therefore hypothesised that the ability to adopt the ϕ and ψ angles of left-handed helical conformations influences the average abundance scores of residues in loop structure. To test our hypothesis, we identified all loop residues with backbone angles in the ϕ,ψ area stated in the above. As expected, many of the identified residues were glycine and asparagine residues, whereas no isoleucine or valine residues in our six protein dataset were found to have this backbone conformation (Fig. 3C). Moreover, for several residue types, we identified only a single residue or no residues with this conformation. We next calculated an average abundance score substitution matrix for the identified residues and moreover averaged the abundance scores for substitutions to each of the twenty amino acids across reference residue types (Fig. 3C). Clearly, substitution to proline, isoleucine, valine and tryptophan are the least favourable substitution types on average, and substitutions to glycine are the most tolerated. Our analysis thus suggests that substitution of loop residues with left-handed helical backbone conformations typically disrupts cellular abundance if this conformation is not usual for the variant residue to adopt.

Finally, we quantified similarities and differences between matrices calculated for residues sitting in different environments and using different subsets of the pooled VAMP-seq dataset, comparing both absolute numbers and correlations (Fig. S17). First, we compared average score substitution matrices calculated by only using data from single proteins and found that some matrices resemble each other more closely that others. In buried environments, the average abundance score for each substitution type generally depends on the protein (Fig. S17A). However, average effects in PTEN, TPMT and CYP2C9 appear somewhat related, and NUDT15, ASPA and PRKN average scores also seem to share certain features. In exposed environments, matrices are generally equally similar, with the exception that average substitution scores in ASPA appear quite different from the averages in all other proteins (Fig. S17B). The datasets thus mainly differ due to differences in substitution effects in buried environments. On the other hand, matrices constructed by leaving out data from individual proteins are relatively similar (Fig. S17C,D). Finally, we found that some matrices calculated using data from all proteins are correlated, such as buried and strand or exposed and loop (Fig. S17E). Buried and exposed are least correlated, making them good (orthogonal) features in the model. Helix and strand matrices correlate and are perhaps both dominated by the residues sitting in buried environments.

Discovering solvent-exposed residues important for cellular stability

In vitro studies have demonstrated that NUDT15 (***Carter et al., 2015***) and ASPA (***Moore et al., 2003***; ***Bitto et al., 2007***; ***Le Coq et al., 2008***) form homodimeric assemblies in solution and when crystallised. In a previous analysis of the NUDT15 VAMP-seq dataset, the homodimer interface present in the NUDT15 crystal structure was found to contain several residue sites at which the mutational tolerance was lower than the average tolerance across all residues and substitutions hence consistently resulted in decreased abundance (***Suiter et al., 2020***). Sensitivity towards substitutions has also been noticed for residues sitting in the monomer-monomer interface found in the ASPA crystal structure (***Grønbæk-Thygesen et al., 2024***). Since prior work thus suggests that NUDT15 and ASPA homodimerisation is important for the maintaining cellular abundance of the proteins, we have used the NUDT15 and ASPA homodimer structures for all analyses described above. However, no quantitative analysis of the mutational tolerance and hence importance for maintaining cellular stability has actually been reported for the interface residues in ASPA, and so to justify our choice, we (re)analysed the crystal structure interfaces of the two proteins using the pooled VAMP-seq dataset.

We specifically examined whether NUDT15 and ASPA homodimerisation might affect the *in vivo* stability of the proteins in the VAMP-seq experiments by quantifying the extent to which the abundance scores of the homodimer interface residues resemble the average substitution scores of buried or solvent-exposed residues. For the analysis, we recalculated the exposure-based substitution matrices using only monomeric structures for the residue classification and leaving out either NUDT15 or ASPA data from the calculation. For every interface residue in the dimer structures, we then calculated the root-mean-square-deviation (RMSD) between all variant abundance scores reported for the interface residue and the average abundance score substitution profile for the interface residue amino acid type in either buried or exposed environments. For all interface residues, we thus obtained two numbers, $RMSD_{exposed}$ and $RMSD_{buried}$, which respectively quantify how closely related the substitution profile scores of the residue are to the average scores of exposed and buried sites (Fig. 4). If the $RMSD_{buried}$ of a residue is smaller than the $RMSD_{exposed}$, we thus expect the residue to be buried in the monomer-monomer interface in the cell, and vice versa.

In NUDT15, the variant abundance scores for 11 out of 13 crystal structure interface residues are more similar to the average abundance scores of buried residues than exposed residues (Fig. 4A). The disruption of the interactions formed by these 11 residues thus reduces the cellular abundance of NUDT15 relatively similarly to how disruption of the interactions of core residues would, suggesting that the 11 residues are buried in the dimer interface inside the cell. Residues L153 and L156 have abundance scores that resemble those of exposed residues more closely than those of buried residues. In the crystal structure of the dimeric assembly of the protein, L153 and L156 are positioned next to each other on the border of the dimer interface (Fig. 4C). While the side chains of the two residues do point into the interface in the static structure, our analysis suggests that they are not more important for the cellular stability of NUDT15 than if they had been sitting in solvent-exposed positions. We note that this result is more clear for residue L153 than residue L156.

Using the same method, we found that 10 out of 14 interface residues in the ASPA dimer have a smaller $RMSD_{buried}$ than $RMSD_{exposed}$ (Fig. 4B). The majority of the ASPA dimer interface residues thus appear structurally buried, and we conclude that ASPA exists as a dimer *in vivo* and that dimerisation is important for maintaining the cellular stability of the protein. In our analysis, we moreover found crystal structure interface residues L25, F29, C61 and L265 to have abundance scores most similar to those of solvent-exposed residues of the same amino acid types. The four residues do not appear to be as critical for ASPA dimerisation and cellular stability as the rest of the interface residues. In the crystal structure, L265 is positioned in a loop at the border of the interface (Fig. 4D), while L25, F29 and C61 are spatially close to each other at a site distant from L265 (Fig. 4E). We note that for ASPA, the $RMSD_{buried}$ for several residues is relatively high although still smaller than

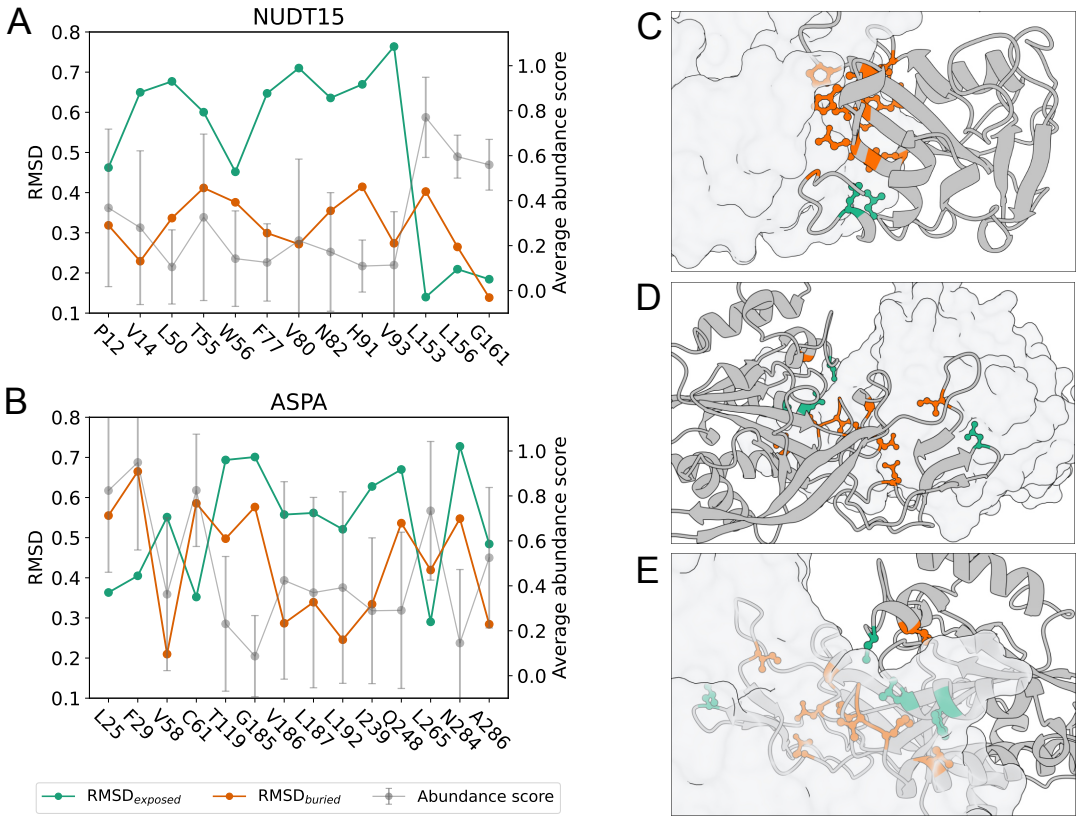

Figure 4. Homodimerisation stabilises NUDT15 and ASPA *in vivo*. RMSD between abundance score substitution profile and average abundance scores in buried (orange) and exposed (green) environments for residues in (A) the NUDT15 dimer interface and (B) the ASPA dimer interface. For each interface residue, the average abundance score (grey) is also shown with error bars that indicate the abundance score standard deviation at the position. If $RMSD_{exposed}$ is smaller than $RMSD_{buried}$, the abundance score substitution profile of the residue resembles the average profile of an exposed residue more than that of a buried residue of the same amino acid type, and vice versa. RMSD values were only calculated for residues with at least five reported abundance scores. (C) NUDT15 dimer with one monomer represented by cartoon of backbone and one monomer shown in transparent surface representation. Side chains are shown for all interface residues, and interface residues with $RMSD_{buried}$ smaller than $RMSD_{exposed}$ are shown in orange, while interface residues with $RMSD_{exposed}$ smaller than $RMSD_{buried}$ are shown in green. (D, E) ASPA dimer shown from two different angles represented similarly to the NUDT15 dimer.

$RMSD_{exposed}$, in accordance with the fact that the ASPA VAMP-seq dataset contains many variants with very low abundance.

Having analysed residues found in the monomer-monomer interfaces of the NUDT15 and ASPA structures, we next tested whether our method was able to identify other solvent-exposed residues with $RMSD_{buried} < RMSD_{exposed}$ on the non-interface surfaces of NUDT15 and ASPA as well as on the surfaces of the four other proteins in our dataset. At the same time, we tested whether any buried residues have $RMSD_{exposed} < RMSD_{buried}$. For the analysis, we used average abundance score matrices for buried and exposed residues calculated using only monomer structures and excluding data from the protein being analysed. For every residue in each of the six proteins, we calculated $RMSD_{exposed}$ and $RMSD_{buried}$ using all reported variant abundance scores for the residue (Fig. S18), as described in the above, allowing us to discover residues for which the structural environment is not necessarily a good indicator of the impact of substitutions on abundance.

Generally, we find many residues to behave as expected, although we identify surface-exposed residues with $RMSD_{buried} < RMSD_{exposed}$ and buried residues with $RMSD_{exposed} < RMSD_{buried}$ in all proteins. The number of residues for which the abundance score substitution profile does not match the average profile for residues in a similar structural environment depends on the protein. We for instance find 51 out of 351 (15%) exposed residues in PRKN to have $RMSD_{buried} < RMSD_{exposed}$ and 17 out of 114 (15%) buried residues in PRKN to have $RMSD_{exposed} < RMSD_{buried}$. In the ASPA monomer, we on the other hand find 89 out of 183 (49%) exposed residues with $RMSD_{buried} < RMSD_{exposed}$ and 18 out of 130 (14%) buried residues with $RMSD_{exposed} < RMSD_{buried}$. The accuracy with which environment indicates mutational tolerance is highest for PRKN and PTEN and lower and relatively similar for TPMT, CYP2C9, NUDT15 and ASPA (Fig. S18). Considering the number of non-interface, surface-exposed residues that we find to have $RMSD_{buried} < RMSD_{exposed}$ in NUDT15 and ASPA (Fig. S18, S19), we cannot exclude that the crystal structure interface residues might be important for maintaining cellular stability in ways that are not just related to the formation of a homodimer.

Given the fact that the six abundance score distributions have considerably different shapes (Fig. S1), some of the identified discrepancies between residue environments and abundance score profiles are perhaps not surprising. For example, since the PTEN abundance score distribution is shifted towards high abundance score values, it makes sense that we identify many residues in PTEN that we structurally classify as buried, but which have a smaller $RMSD_{exposed}$ than $RMSD_{buried}$ value. The opposite might be true for solvent-exposed residues in for example ASPA and PRKN that appear to have abundance score substitution profiles most similar to the average profile of buried residues. As discussed under *Overview of VAMP-seq datasets*, a number of factors likely contribute to producing the different score distributions, and these factors will thereby likely also give rise to some of the identified mismatches between structural environment and substitution profiles. In spite of this, we have shown in the above that our method is able to identify surface residues for which the mismatches likely are indicators of residues with functions (in this case dimerisation) important for abundance.

In line with this, we focus the rest of our analysis specifically on solvent-exposed residues for which the $RMSD_{buried}$ is smaller than $RMSD_{exposed}$, thereby generating hypotheses regarding which exposed residues might be required for maintaining cellular abundance of the proteins. We mapped this group of residues onto the protein structures (Fig. S19) and indeed found that our method works not only for analysis of residues likely involved in homodimerisation, but also for revealing exposed residues that through different types of biochemistry control abundance. In PRKN, solvent-exposed residues with $RMSD_{buried} < RMSD_{exposed}$ for example include many of the Zn^{2+}-coordinating cysteine residues that are critical for maintaining abundance (***Clausen et al., 2024***). Our method also identifies that the substitution profile of the solvent-exposed S109 in PRKN is more similar to that of buried than exposed serines, which is in line with the fact that certain mutations of this residue are thought to introduce a solvent-exposed quality control degron in the protein (***Clausen et al., 2024***). Finally, the method appears to be able to capture that certain phos-

phorylation sites are important for maintaining abundance. Specifically, it has been shown that residues S380, T382, T383 and S385 of PTEN are phosphorylated in the cell and that mutation of the first three residues to alanine increase the cellular degradation rate of the protein (***Vazquez et al., 2000***). With our method, we identify two of these sites, T383 and S385, to have $RMSD_{buried} < RMSD_{exposed}$ while being exposed in the static structure. The importance of residue S385 has also been discussed in a previous analysis of the VAMP-seq data (***Matreyek et al., 2018***). Since residues S380 and T382 both have less than five reported abundance scores, we did not assess whether our method picks up on these sites as being important for maintaining abundance or not.

In the above, we have thus demonstrated that the $RMSD_{buried}$ and $RMSD_{exposed}$ values of a residue, which respectively measure the similarity between the substitution profile of the residue and the average substitution profiles of buried and exposed residues, can be used to (*i*) tell apart experimentally relevant from irrelevant structures and (*ii*) reveal residue sites with importance for maintaining cellular protein stability, thereby generating hypotheses for further studies. The approach introduced here is related to other methods that similarly use discrepancies between structure data and single residue substitution mutagenesis data to distinguish correct or relevant structures from decoy or wrongly predicted structures (***Adkar et al., 2012***; ***Chiasson et al., 2020***; ***Zutz et al., 2021***), and to methods that aim to derive three-dimensional structures using data generated by MAVEs (***Schmiedel and Lehner, 2019***; ***Rollins et al., 2019***; ***Drake et al., 2024***).

Conclusions

Several previous studies have combined heterogeneous mutagenesis data from multiple MAVEs to analyse amino acid residue substitution effects across proteins in a general manner. In this study, we have similarly analysed a combination of six large mutagenesis datasets, however restricting our analysis to a more homogenous set of MAVE data that were all collected with the VAMP-seq method and report on the impact of substitutions on protein cellular abundance. Our results therefore reveal trends in substitution effects for a single molecular phenotype. We have analysed in total 31,614 single residue substitution variant abundance scores in a structure-based fashion through construction of amino acid substitution matrices reporting on the average abundance scores for all possible substitution types.

We found that, by using simple structural considerations, it is possible to construct structure context-specific substitution matrices that with relatively high accuracy, at least considering the model simplicity, can predict the impact of residue substitutions on cellular abundance in new proteins. We have moreover shown that these matrices are not only of use for prediction tasks, but also allows for discrimination between experimentally, in this case cellularly, relevant and irrelevant protein structures. We propose that the method we have introduced for the last-mentioned purpose is applicable not only for selecting between monomer and dimer structures as done here, but that it might also be useful in a broader context, for example for selecting between correctly and incorrectly predicted structures.

Our large-scale analysis moreover revealed that the average substitution effects for the abundance phenotype to a large extent are in agreement with what one would expected from basic biochemical considerations. In clustering analyses of average amino acid substitution profiles, the amino acids tend to group together according to physicochemical properties, although with noteworthy exceptions, such as for example the extreme substitutional intolerance of aspartate in buried environments. Moreover, while some structural considerations can help rationalise certain abundance variant effects, like those observed in loop residues with dihedral angles similar to those of left-handed helix, this is not always the case, as revealed by the lack of correlation between secondary structure propensity scales and average abundance scores in the corresponding structure type. Given the overall consistency between average abundance score substitution profiles and biochemical expectation, these averages might generally be useful references for how residue substitutions will likely affect cellular abundance. While the combined analysis of the six individual VAMP-seq datasets proved useful in this work, future work developing for example prediction

methods for variant abundance might benefit from more elaborate considerations regarding and treatment of the experimental and biochemical factors that possibly influence the absolute values of the VAMP-seq variant abundance scores.

Methods

VAMP-seq data collection and preparation

We obtained VAMP-seq abundance scores and abundance score standard deviations directly from the original VAMP-seq publications (***Matreyek et al., 2018***, ***2021***; ***Amorosi et al., 2021***; ***Suiter et al., 2020***; ***Grønbæk-Thygesen et al., 2024***; ***Clausen et al., 2024***). We filtered the datasets to include only single residue substitution scores in our analysis, that is, we excluded data for synonymous and nonsense variants. We did not perform any additional quality filtering of the data beyond filtering already performed in the original publications, meaning that scores from positions with low mutational depth are included in our analysis. Moreover, since abundance scores were already normalised in the original VAMP-seq work, we used reported scores without further normalisation. PTEN VAMP-seq data has been measured multiple times to increase the mutational completeness of the variant abundance dataset (***Matreyek et al., 2018***, ***2021***). In our analysis, we used the most recently published PTEN dataset, which is based on a combination of abundance scores measured in the original and updated PTEN work (***Matreyek et al., 2021***). Finally, we excluded variant abundance scores for the first 28 residues of CYP2C9 from all analyses, since the CYP2C9 N-terminal is a transmembrane helix (***Amorosi et al., 2021***).

Quantification of dataset noise levels

We quantified the noise levels in the individual datasets using a bootstrapping approach in which we resampled each VAMP-seq dataset 100 times. Each abundance score was resampled from a Gaussian distribution with mean equal to the originally reported abundance score and standard deviation equal to the reported standard deviation of the score. We calculated r between the originally reported abundance scores and each resampled sets of scores and reported the average of the resulting 100 r values in Figure 1E. We note that abundance score standard deviations are based on a different number of replicate measurements, both within and across datasets, and that our bootstrapped r values do not in all cases correspond to the correlations between replicate experiments reported in the original VAMP-seq publications, with deviations in particular for TPMT and CYP2C9, where our quantification of the noise levels gives higher numbers for r.

Structure preparation and visualisation

We used combined crystal and AlphaFold2 structures (***Jumper et al., 2021***) in our analysis so that our structural input preserved crystal structure coordinates where possible and at the same time had no missing residues. We created the combined structures by first aligning crystal structures and AlphaFold2 structures using the Matchmaker tool in UCSF ChimeraX (v1.3, ***Pettersen et al.*** (***2021***)) and then filled out gaps from missing residues in the crystal structure files with coordinates from the AlphaFold2 structures. We then ran the "alphafold2_ptm" model in ColabFold (v1.5.2, ***Mirdita et al.*** (***2022***)) with the combined structures as input template structures using UniProt sequences as query sequences (Table S1). We specified to not use a multiple sequence alignment for the structure prediction and otherwise used default setting, including omission of Amber relaxation. We verified that the first ranked ColabFold output structures mostly preserved the crystal structure backbone conformations and then used these structures as inputs for all of our analyses. We took this approach to include as much structural information as possible in our modelling while at the same time making sure that our input structures resembled the crystal structures in cases where crystal and AlphaFold2 structures deviated with respect to backbone conformation.

The AlphaFold2 structures that we used as input for this approach were predicted with the AlphaFold Monomer v2.0 pipeline and downloaded from the AlphaFold Protein Structure Database

(***Varadi et al., 2022***), except for in the cases of NUDT15 and ASPA, since these proteins can be found only in their monomeric form in the database. We created the homodimeric assemblies of the proteins with the multimer pipeline "alphafold2_multimer_v3" in ColabFold using default settings, including template mode "pdb70" and MSA mode "mmseqs2_uniref_env". The top ranked dimer structures generated with this approach were then used as input AlphaFold2 structures for the procedure described in the above.

We processed structure data files with pdb-tools (v2.4.3, ***Rodrigues et al.*** (***2018***)). Our structure processing included removal of chains not noted in Table S1 and removal of all HETATM entries in the crystal structure files. All our analyses were thus performed without accounting for co-factors or ions bound to the proteins in their crystal structures. We moreover removed the 28 N-terminal residues of the CYP2C9 structure, as the N-terminal of CYP2C9 is known to form a transmembrane helix (***Amorosi et al., 2021***). In calculations that rely on the monomeric structures of NUDT15 and ASPA, we always used chain A in its conformation in the dimeric structure. All protein structure visualisations were created with ChimeraX.

Calculation of structural features

We used DSSP (***Kabsch and Sander, 1983***) for secondary structure assignment and calculation of solvent accessible surface area for every residue in the wild-type protein structures. Solvent accessible surface area was normalised to obtain relative solvent accessibility using a theoretically derived maximum accessibility per residue (***Tien et al., 2013***). As in other studies (***Hovmöller et al., 2002***), we used secondary structure assignments from DSSP to classify residues into three secondary structure categories, specifically helix (α-, 3_{10}- and π-helix), strand (extended stand and isolated β-bridge) and loop (hydrogen-bonded turn, bend and irregular/loop). These definitions were used throughout our work, except in the analysis of abundance score correlations with helix propensity scales (Fig. S16), where we only included data for α-helical residues.

We also evaluated contact formation between residues by calculating a WCN for every residue in their wild-type structure environments. Specifically, the WCN for every residue i was calculated as a function of the distances $r_{i,j}$ to all other residues in the protein structure according to the equation

$$\mathrm{WCN}_i = \sum_{j \neq i} s(r_{i,j}) \quad \text{with} \quad s(r) = \frac{1 - \left(\frac{r}{r_0}\right)^6}{1 - \left(\frac{r}{r_0}\right)^{12}}, \tag{1}$$

in which we set r_0 = 7 Å. We defined the distance between two residues to be the shortest distance between any pair of heavy atoms in the side chains, except if one residue involved was glycine, in which case we used the shortest distance between any interresidue atom pair. Distances were calculated with the MDTraj (v1.9.7, (***McGibbon et al., 2015***)) function compute_contacts.

Definitions of buried and exposed residues

We classified residues with an rASA smaller than or equal to 0.1 as structurally buried and residues with an rASA larger than 0.1 as solvent-exposed. The 0.1 cutoff value was selected using a grid search in which we scanned combinations of rASA and WCN values to maximise the average correlation between experimental abundance scores and abundance scores predicted with the exposure-based substitution matrices containing average abundance scores. More specifically, we calculated the two substitution matrices using a range of rASA and WCN cutoff combinations to classify residues as buried or exposed. rASA values from 0 to 0.5 were scanned together with WCN values from 0 to 20. We defined buried residues as residues with a WCN larger than or equal to the WCN cutoff value *and* an rASA smaller than or equal to the rASA cutoff value. Residues not classified

as buried were classified as exposed, meaning that exposed residues would have a WCN smaller than the WCN cutoff or an rASA larger than the rASA cutoff.

For each combination of rASA and WCN cutoff values, we tested the predictive power of the substitution matrices using leave-one-protein-out cross-validation, that is, we calculated the matrices for each cutoff combination leaving out of one the six proteins and then attempted to predict the abundance scores for the omitted protein. We calculated r and the mean absolute error (MAE) between experimental and predicted abundance scores for each protein and then averaged results across proteins. We found that, on average, an rASA cutoff of 0.1 maximises r and minimises the MAE when used in combination with WCN cutoff values of 0, 5 and 10, however with no considerable difference between the three WCN cutoffs (Fig. S6A,B). A WCN cutoff value of 0 effectively corresponds to applying only the rASA cutoff. For simplicity, we therefore used an rASA cutoff of 0.1 and did not consider WCN for exposure-based residue classifications in the rest of the analyses in this work.

Calculation of ΔΔG values with Rosetta

We calculated the difference in Gibbs folding free energy between wild-type proteins and all possible single residue substitution variants ($\Delta\Delta G = \Delta G_{variant} - \Delta G_{wild\ type}$) with Rosetta using the cartesian_ddg protocol and *opt-nov15* energy function (***Park et al., 2016***). We used an in-house pipeline (https://github.com/KULL-Centre/PRISM/tree/main/software/rosetta_ddG_pipeline, v0.2.1) to first prepare and relax input structures and then calculate energies, which we converted from Rosetta energy units (REU) to kcal/mol with the conversion factor 2.9 REU/(kcal/mol) (***Park et al., 2016***). For evaluation of the effect of a given substitution in dimeric structures, we made the residue substitution in both monomers simultaneously and obtained a ΔΔG for the dimer, which we divided by 2 to get the stability change per residue.

Hierarchical clustering and principal component analysis

Hierarchical clustering of substitution matrix rows and columns was performed and visualised using the seaborn function clustermap. We set function parameters method='average' and metric='euclidean', meaning that distances between clusters were evaluated by calculating the average distance between all pairs of elements in the clusters using the Euclidean distance as distance metric. Prior to performing the clustering, we set the average abundance scores for synonymous substitutions equal to one.

We performed PCA of abundance scores averages for residues in buried and exposed environments by constructing, for each environment type, a 20x40 matrix that for each of the 20 amino acid types specified the 40 abundance score averages for all substitutions to and from that amino acid residue type. In the reformatted matrices, we set scores for synonymous substitutions equal to one. We then used the scikit-learn class sklearn.decomposition. PCA with default parameters to perform the PCA. The input features were not scaled prior to the analysis.

Analysis of substitution matrices for helix- and loop-forming residues

We tested the correlation between average abundance score matrices for residues forming α-helix using a number of different helix propensity scales (***Pace and Scholtz, 1998***; ***Rohl et al., 1996***; ***Muñoz and Serrano, 1995***; ***Chou and Fasman, 1978***; ***Williams et al., 1987***; ***Luque et al., 1996***). The scales all report on the residue ΔΔG relative to alanine for helix formation. All numbers for our analysis were taken from a single paper which compared six different helix propensity scales (***Pace and Scholtz, 1998***), and we have here followed the naming of the scales presented in that paper. To test the correlation with our average abundance score matrices, we calculated a helix propensity substitution matrix for each helix propensity scale by subtracting the ΔΔG of the variant residue from the ΔΔG of the reference residue. We then calculated the correlation coefficient between the helix propensity and the average abundance score substitution matrices. For this analysis, we used average abundance score matrices constructed with abundance scores only for residues forming

α-helix, unlike in all our other analyses in this paper, where our helix matrices includes data from residues forming α-helix as well as 3_{10}- and π-helix

To analyse the substitution patterns of loop residues adopting backbone conformations similar to those found in left-handed helices, we used the MDTraj functions compute_phi and compute_psi to identify all loop residues for which the backbone ϕ and ψ angles simultaneously fell within the ranges $0° < \phi < 180°$ and $-90° < \psi < 90°$ (***Hovmöller et al., 2002***). We excluded residues that were not present in the crystal structures of the proteins from this analysis to make sure that wrongly predicted loop residue conformations from AlphaFold2 did not influence the results.

Analysis of solvent-exposed residues important for cellular stability

For our analysis of NUDT15 and ASPA homodimerisation, we defined homodimer interface residues as residues that were classified as exposed in the monomer structures and as buried in the dimer structures. To filter out residues which experience minor changes in rASA upon dimerisation, but still change category with the strict 0.1 rASA cutoff used to distinguish between buried and exposed residues, we only included residues in the interface residue category if the change in rASA was more than 0.01 when going from monomer to dimer.

For the analysis of the homodimer interfaces as well as for the analysis of the substitution profiles for all remaining residues in the six proteins, we calculated $\text{RMSD}_{\text{buried}}$ and $\text{RMSD}_{\text{exposed}}$ values only for residue positions for which at least five abundance scores were reported in the experimental datasets. In our results, we thus show no $\text{RMSD}_{\text{buried}}$ and $\text{RMSD}_{\text{exposed}}$ data for any residues with fewer than five abundance scores. We note that all NUDT15 interface residues have at least five abundance scores and that all ASPA interface residues except one (residue 242) have at least five abundance scores.

Availability of data and code

Data and code for reproducing the results presented in this work are available at https://github.com/KULL-Centre/_2024_Schulze_abundance-analysis.

Acknowledgements

This work was funded by the Novo Nordisk Foundation challenge program PRISM (Protein Interactions and Stability in Medicine and Genomics, NNF18OC0033950, to K.L.-L.). We thank Lene Clausen, Martin Grønbæk-Thygesen, Vasileios Voutsinos, Kristoffer E. Johansson, Matteo Cagiada, Amelie Stein, and Rasmus Hartmann-Petersen and other members of the PRISM centre for productive discussions and suggestions on the topic of protein abundance. We acknowledge access to computational resources at the Biocomputing Core Facility at the Department of Biology, University of Copenhagen.

Competing interests

KL-L holds stock options in and is a consultant for Peptone Ltd.

References

Abildgaard AB, Stein A, Nielsen SV, Schultz-Knudsen K, Papaleo E, Shrikhande A, Hoffmann ER, Bernstein I, Gerdes AM, Takahashi M, Ishioka C, Lindorff-Larsen K, Hartmann-Petersen R. Computational and cellular studies reveal structural destabilization and degradation of MLH1 variants in Lynch syndrome. eLife. 2019 Nov; 8:e49138.

Adkar BV, Tripathi A, Sahoo A, Bajaj K, Goswami D, Chakrabarti P, Swarnkar MK, Gokhale RS, Varadarajan R. Protein Model Discrimination Using Mutational Sensitivity Derived from Deep Sequencing. Structure. 2012 Feb; 20(2):371–381.

Amorosi CJ, Chiasson MA, McDonald MG, Wong LH, Sitko KA, Boyle G, Kowalski JP, Rettie AE, Fowler DM, Dunham MJ. Massively parallel characterization of CYP2C9 variant enzyme activity and abundance. The American Journal of Human Genetics. 2021 Sep; 108(9):1735–1751.

Beltran T, Jiang X, Shen Y, Lehner B. Site saturation mutagenesis of 500 human protein domains reveals the contribution of protein destabilization to genetic disease. bioRxiv. 2024 Apr; .

Bitto E, Bingman CA, Wesenberg GE, McCoy JG, Phillips GN. Structure of aspartoacylase, the brain enzyme impaired in Canavan disease. Proceedings of the National Academy of Sciences. 2007 Jan; 104(2):456–461.

Cagiada M, Johansson KE, Valanciute A, Nielsen SV, Hartmann-Petersen R, Yang JJ, Fowler DM, Stein A, Lindorff-Larsen K. Understanding the Origins of Loss of Protein Function by Analyzing the Effects of Thousands of Variants on Activity and Abundance. Molecular Biology and Evolution. 2021 Jul; 38(8):3235–3246.

Cagiada M, Jonsson N, Lindorff-Larsen K. Decoding molecular mechanisms for loss of function variants in the human proteome. bioRxiv. 2024 May; .

Caldararu O, Blundell TL, Kepp KP. Three Simple Properties Explain Protein Stability Change upon Mutation. Journal of Chemical Information and Modeling. 2021 Apr; 61(4):1981–1988.

Carter M, Jemth AS, Hagenkort A, Page BDG, Gustafsson R, Griese JJ, Gad H, Valerie NCK, Desroses M, Boström J, Warpman Berglund U, Helleday T, Stenmark P. Crystal structure, biochemical and cellular activities demonstrate separate functions of MTH1 and MTH2. Nature Communications. 2015 Aug; 6(1):7871.

Chakravarty S, Varadarajan R. Residue depth: a novel parameter for the analysis of protein structure and stability. Structure. 1999 Jul; 7(7):723–732.

Chiasson MA, Rollins NJ, Stephany JJ, Sitko KA, Matreyek KA, Verby M, Sun S, Roth FP, DeSloover D, Marks DS, Rettie AE, Fowler DM. Multiplexed measurement of variant abundance and activity reveals VKOR topology, active site and human variant impact. eLife. 2020 Sep; 9:e58026.

Chou PY, Fasman GD. Empirical Predictions of Protein Conformation. Annual Review of Biochemistry. 1978; 47(Volume 47, 1978):251–276.

Cisneros AF, Gagnon-Arsenault I, Dubé AK, Després PC, Kumar P, Lafontaine K, Pelletier JN, Landry CR. Epistasis between promoter activity and coding mutations shapes gene evolvability. Science Advances. 2023; 9(5):eadd9109.

Clausen L, Voutsinos V, Cagiada M, Johansson KE, Grønbæk-Thygesen M, Nariya S, Powell RL, Have MKN, Oestergaard VH, Stein A, Fowler DM, Lindorff-Larsen K, Hartmann-Petersen R. A mutational atlas for Parkin proteostasis. Nature Communications. 2024 Feb; 15(1):1541.

Cota E, Hamill SJ, Fowler SB, Clarke J. Two proteins with the same structure respond very differently to mutation: the role of plasticity in protein stability. Journal of Molecular Biology. 2000 Sep; 302(3):713–725.

Dang CC, Minh BQ, Mcshea H, Masel J, James JE, Sy L, Lanfear R. nQMaker: Estimating Time Nonreversible Amino Acid Substitution Models. Systematic Biology. 2022; 71.

Dayhoff M, Schwartz R, Orcutt B. A model of evolutionary change in proteins. Atlas of protein sequence and structure. 1978; 5:345–352.

Drake ZC, Day E, Toth P, Lindert S. Deep-Learning Structure Elucidation from Single-Mutant Deep Mutational Scanning. bioRxiv. 2024 May; .

Dunham AS, Beltrao P. Exploring amino acid functions in a deep mutational landscape. Molecular Systems Biology. 2021 Jul; 17(7):e10305.

Esposito D, Weile J, Shendure J, Starita LM, Papenfuss AT, Roth FP, Fowler DM, Rubin AF. MaveDB: an open-source platform to distribute and interpret data from multiplexed assays of variant effect. Genome Biology. 2019 Dec; 20(1):223.

Faure AJ, Domingo J, Schmiedel JM, Hidalgo-Carcedo C, Diss G, Lehner B. Mapping the energetic and allosteric landscapes of protein binding domains. Nature. 2022 Apr; 604(7904):175–183.

Fowler DM, Fields S. Deep mutational scanning: a new style of protein science. Nature Methods. 2014 Aug; 11(8):801–807.

Fowler DM, Stephany JJ, Fields S. Measuring the activity of protein variants on a large scale using deep mutational scanning. Nature Protocols. 2014 Sep; 9(9):2267–2284.

Geck RC, Boyle G, Amorosi CJ, Fowler DM, Dunham MJ. Measuring Pharmacogene Variant Function at Scale Using Multiplexed Assays. Annual Review of Pharmacology and Toxicology. 2022 Jan; 62(1):531–550.

Gerasimavicius L, Livesey BJ, Marsh JA. Correspondence between functional scores from deep mutational scans and predicted effects on protein stability. Protein Science. 2023 Jul; 32(7):e4688.

Gray VE, Hause RJ, Fowler DM. Analysis of Large-Scale Mutagenesis Data To Assess the Impact of Single Amino Acid Substitutions. Genetics. 2017 Sep; 207(1):53–61.

Grønbæk-Thygesen M, Voutsinos V, Johansson KE, Schulze TK, Cagiada M, Pedersen L, Clausen L, Nariya S, Powell RL, Stein A, Fowler DM, Lindorff-Larsen K, Hartmann-Petersen R. Deep mutational scanning reveals a correlation between degradation and toxicity of thousands of aspartoacylase variants. Nature Communications. 2024 May; 15(1):4026.

Henikoff S, Henikoff JG. Amino acid substitution matrices from protein blocks. Proceedings of the National Academy of Sciences. 1992 Nov; 89(22):10915–10919.

Hovmöller S, Zhou T, Ohlson T. Conformations of amino acids in proteins. Acta Crystallographica Section D Biological Crystallography. 2002 May; 58(5):768–776.

Høie MH, Cagiada M, Beck Frederiksen AH, Stein A, Lindorff-Larsen K. Predicting and interpreting large-scale mutagenesis data using analyses of protein stability and conservation. Cell Reports. 2022 Jan; 38(2):110207.

Jiang L, Mishra P, Hietpas RT, Zeldovich KB, Bolon DNA. Latent Effects of Hsp90 Mutants Revealed at Reduced Expression Levels. PLoS Genetics. 2013 Jun; 9(6):e1003600.

Jumper J, Evans R, Pritzel A, Green T, Figurnov M, Ronneberger O, Tunyasuvunakool K, Bates R, Žídek A, Potapenko A, Bridgland A, Meyer C, Kohl SAA, Ballard AJ, Cowie A, Romera-Paredes B, Nikolov S, Jain R, Adler J, Back T, et al. Highly accurate protein structure prediction with AlphaFold. Nature. 2021 Aug; 596(7873):583–589.

Kabsch W, Sander C. Dictionary of protein secondary structure: Pattern recognition of hydrogen-bonded and geometrical features. Biopolymers. 1983 Dec; 22(12):2577–2637.

Kumar A, Aguirre JD, Condos TE, Martinez-Torres RJ, Chaugule VK, Toth R, Sundaramoorthy R, Mercier P, Knebel A, Spratt DE, Barber KR, Shaw GS, Walden H. Disruption of the autoinhibited state primes the E3 ligase parkin for activation and catalysis. The EMBO Journal. 2015 Oct; 34(20):2506–2521.

Le Coq J, Pavlovsky A, Malik R, Sanishvili R, Xu C, Viola RE. Examination of the Mechanism of Human Brain Aspartoacylase through the Binding of an Intermediate Analogue ·. Biochemistry. 2008 Mar; 47(11):3484–3492.

Lee JO, Yang H, Georgescu MM, Cristofano AD, Maehama T, Shi Y, Dixon JE, Pandolfi P, Pavletich NP. Crystal Structure of the PTEN Tumor Suppressor: Implications for Its Phosphoinositide Phosphatase Activity and Membrane Association. Cell. 1999; .

Luque I, Mayorga OL, Freire E. Structure-Based Thermodynamic Scale of α-Helix Propensities in Amino Acids. Biochemistry. 1996 Jan; 35(42):13681–13688. Publisher: American Chemical Society.

Marrero MC, Barrio-Hernandez I. Toward Understanding the Biochemical Determinants of Protein Degradation Rates. ACS Omega. 2021 Mar; 6(8):5091–5100.

Matreyek KA, Starita LM, Stephany JJ, Martin B, Chiasson MA, Gray VE, Kircher M, Khechaduri A, Dines JN, Hause RJ, Bhatia S, Evans WE, Relling MV, Yang W, Shendure J, Fowler DM. Multiplex assessment of protein variant abundance by massively parallel sequencing. Nature Genetics. 2018 Jun; 50(6):874–882.

Matreyek KA, Stephany JJ, Ahler E, Fowler DM. Integrating thousands of PTEN variant activity and abundance measurements reveals variant subgroups and new dominant negatives in cancers. Genome Medicine. 2021 Dec; 13(1):165.

Mavor D, Barlow K, Thompson S, Barad BA, Bonny AR, Cario CL, Gaskins G, Liu Z, Deming L, Axen SD, Caceres E, Chen W, Cuesta A, Gate RE, Green EM, Hulce KR, Ji W, Kenner LR, Mensa B, Morinishi LS, et al. Determination of ubiquitin fitness landscapes under different chemical stresses in a classroom setting. eLife. 2016 Apr; 5:e15802.

Mavor D, Barlow KA, Asarnow D, Birman Y, Britain D, Chen W, Green EM, Kenner LR, Mensa B, Morinishi LS, Nelson CA, Poss EM, Suresh P, Tian R, Arhar T, Ary BE, Bauer DP, Bergman ID, Brunetti RM, Chio CM, et al. Extending chemical perturbations of the ubiquitin fitness landscape in a classroom setting reveals new constraints on sequence tolerance. Biology Open. 2018 Jul; 7(7):bio036103.

McGibbon RT, Beauchamp KA, Harrigan MP, Klein C, Swails JM, Hernández CX, Schwantes CR, Wang LP, Lane TJ, Pande VS. MDTraj: A Modern Open Library for the Analysis of Molecular Dynamics Trajectories. Biophysical Journal. 2015; 109(8):1528 – 1532.

Mirdita M, Schütze K, Moriwaki Y, Heo L, Ovchinnikov S, Steinegger M. ColabFold: making protein folding accessible to all. Nature Methods. 2022 Jun; 19(6):679–682.

Moore RA, Le Coq J, Faehnle CR, Viola RE. Purification and preliminary characterization of brain aspartoacylase. Archives of Biochemistry and Biophysics. 2003 May; 413(1):1–8.

Munro D, Singh M. DeMaSk: a deep mutational scanning substitution matrix and its use for variant impact prediction. Bioinformatics. 2021 Apr; 36(22-23):5322–5329.

Muñoz V, Serrano L. Elucidating the Folding Problem of Helical Peptides using Empirical Parameters. II†. Helix Macrodipole Effects and Rational Modification of the Helical Content of Natural Peptides. Journal of Molecular Biology. 1995 Jan; 245(3):275–296.

Nguyen TN, Ingle C, Thompson S, Reynolds KA. The genetic landscape of a metabolic interaction. Nature Communications. 2024 Apr; 15(1):3351.

Nielsen SV, Stein A, Dinitzen AB, Papaleo E, Tatham MH, Poulsen EG, Kassem MM, Rasmussen LJ, Lindorff-Larsen K, Hartmann-Petersen R. Predicting the impact of Lynch syndrome-causing missense mutations from structural calculations. PLOS Genetics. 2017 Apr; 13(4):e1006739.

Pace CN, Scholtz JM. A Helix Propensity Scale Based on Experimental Studies of Peptides and Proteins. Biophysical Journal. 1998 Jul; 75(1):422–427.

Park H, Bradley P, Greisen P, Liu Y, Mulligan VK, Kim DE, Baker D, DiMaio F. Simultaneous Optimization of Biomolecular Energy Functions on Features from Small Molecules and Macromolecules. Journal of Chemical Theory and Computation. 2016 Dec; 12(12):6201–6212.

Peterman N, Levine E. Sort-seq under the hood: implications of design choices on large-scale characterization of sequence-function relations. BMC Genomics. 2016 Dec; 17(1):206.

Pettersen EF, Goddard TD, Huang CC, Meng EC, Couch GS, Croll TI, Morris JH, Ferrin TE. UCSF ChimeraX: Structure visualization for researchers, educators, and developers. Protein Science. 2021 Jan; 30(1):70–82.

Ribeiro AJM, Tyzack JD, Borkakoti N, Holliday GL, Thornton JM. A global analysis of function and conservation of catalytic residues in enzymes. Journal of Biological Chemistry. 2020 Jan; 295(2):314–324.

Rocklin GJ, Chidyausiku TM, Goreshnik I, Ford A, Houliston S, Lemak A, Carter L, Ravichandran R, Mulligan VK, Chevalier A, Arrowsmith CH, Baker D. Global analysis of protein folding using massively parallel design, synthesis, and testing. Science. 2017 Jul; 357(6347):168–175.

Rodrigues J, Teixeira J, Trellet M, Bonvin A. pdb-tools: a swiss army knife for molecular structures [version 1; peer review: 2 approved]. F1000Research. 2018; 7(1961).

Rohl CA, Chakrabartty A, Baldwin RL. Helix propagation and N-cap propensities of the amino acids measured in alanine-based peptides in 40 volume percent trifluoroethanol. Protein Science. 1996 Dec; 5(12):2623–2637.

Rollins NJ, Brock KP, Poelwijk FJ, Stiffler MA, Gauthier NP, Sander C, Marks DS. Inferring protein 3D structure from deep mutation scans. Nature Genetics. 2019 Jul; 51(7):1170–1176.

Rubin AF, Gelman H, Lucas N, Bajjalieh SM, Papenfuss AT, Speed TP, Fowler DM. A statistical framework for analyzing deep mutational scanning data. Genome Biology. 2017 Dec; 18(1):150.

Rubin AF, Min JK, Rollins NJ, Da EY, Esposito D, Harrington M, Stone J, Bianchi AH, Dias M, Frazer J, Fu Y, Gallaher M, Li I, Moscatelli O, Ong JY, Rollins JE, Wakefield MJ, "Sunny" Ye S, Tam A, McEwen AE, et al. MaveDB v2: a curated community database with over three million variant effects from multiplexed functional assays. bioRxiv. 2021 Nov; .

Scheller R, Stein A, Nielsen SV, Marin FI, Gerdes A, Marco M, Papaleo E, Lindorff-Larsen K, Hartmann-Petersen R. Toward mechanistic models for genotype–phenotype correlations in phenylketonuria using protein stability calculations. Human Mutation. 2019 Apr; 40(4):444–457.

Schmiedel JM, Lehner B. Determining protein structures using deep mutagenesis. Nature Genetics. 2019 Jul; 51(7):1177–1186.

Serrano L, Jr JTK, Cann P, Matouschek A, Fersht AR. The Folding of an Enzyme II. Substructure of Barnase and the Contribution of Different Interactions to Protein Stability. Journal of Molecular Biology. 1992; 224:783–804.

Suiter CC, Moriyama T, Matreyek KA, Yang W, Scaletti ER, Nishii R, Yang W, Hoshitsuki K, Singh M, Trehan A, Parish C, Smith C, Li L, Bhojwani D, Yuen LYP, Li Ck, Li Ch, Yang Yl, Walker GJ, Goodhand JR, et al. Massively parallel variant characterization identifies *NUDT15* alleles associated with thiopurine toxicity. Proceedings of the National Academy of Sciences. 2020 Mar; 117(10):5394–5401.

Tabet D, Parikh V, Mali P, Roth FP, Claussnitzer M. Scalable Functional Assays for the Interpretation of Human Genetic Variation. Annual Review of Genetics. 2022 Nov; 56(1):441–465.

Thompson S, Zhang Y, Ingle C, Reynolds KA, Kortemme T. Altered expression of a quality control protease in E. coli reshapes the in vivo mutational landscape of a model enzyme. Elife. 2020; 9:e53476.

Tien MZ, Meyer AG, Sydykova DK, Spielman SJ, Wilke CO. Maximum Allowed Solvent Accessibilites of Residues in Proteins. PLoS ONE. 2013 Nov; 8(11):e80635.

Tsuboyama K, Dauparas J, Chen J, Laine E, Mohseni Behbahani Y, Weinstein JJ, Mangan NM, Ovchinnikov S, Rocklin GJ. Mega-scale experimental analysis of protein folding stability in biology and design. Nature. 2023 Aug; 620(7973):434–444.

Varadi M, Anyango S, Deshpande M, Nair S, Natassia C, Yordanova G, Yuan D, Stroe O, Wood G, Laydon A, Žídek A, Green T, Tunyasuvunakool K, Petersen S, Jumper J, Clancy E, Green R, Vora A, Lutfi M, Figurnov M, et al. AlphaFold Protein Structure Database: massively expanding the structural coverage of protein-sequence space with high-accuracy models. Nucleic Acids Research. 2022 Jan; 50(D1):D439–D444.

Vazquez F, Ramaswamy S, Nakamura N, Sellers WR. Phosphorylation of the PTEN Tail Regulates Protein Stability and Function. Molecular and Cellular Biology. 2000 Jul; 20(14):5010–5018.

Weile J, Kishore N, Sun S, Maaieh R, Verby M, Li R, Fotiadou I, Kitaygorodsky J, Wu Y, Holenstein A, et al. Shifting landscapes of human MTHFR missense-variant effects. The American Journal of Human Genetics. 2021; 108(7):1283–1300.

Weile J, Roth FP. Multiplexed assays of variant effects contribute to a growing genotype–phenotype atlas. Human Genetics. 2018 Sep; 137(9):665–678.

Wester MR, Yano JK, Schoch GA, Yang C, Griffin KJ, Stout CD, Johnson EF. The Structure of Human Cytochrome P450 2C9 Complexed with Flurbiprofen at 2.0-Å Resolution. Journal of Biological Chemistry. 2004 Aug; 279(34):35630–35637.

Williams RW, Chang A, Juretić D, Loughran S. Secondary structure predictions and medium range interactions. Biochimica et Biophysica Acta (BBA) - Protein Structure and Molecular Enzymology. 1987 Nov; 916(2):200–204.

Wu H, Horton JR, Battaile K, Allali-Hassani A, Martin F, Zeng H, Loppnau P, Vedadi M, Bochkarev A, Plotnikov AN, Cheng X. Structural basis of allele variation of human thiopurine-*S*-methyltransferase. Proteins: Structure, Function, and Bioinformatics. 2007 Apr; 67(1):198–208.

Yampolsky LY, Stoltzfus A. The Exchangeability of Amino Acids in Proteins. Genetics. 2005 Aug; 170(4):1459–1472.

Zutz A, Hamborg L, Pedersen LE, Kassem MM, Papaleo E, Koza A, Herrgård MJ, Jensen SI, Teilum K, Lindorff-Larsen K, Nielsen AT. A dual-reporter system for investigating and optimizing protein translation and folding in E. coli. Nature Communications. 2021 Oct; 12(1):6093.

Protein name	Abbreviation	UniProt ID	PDB ID	PDB chain	Residues
Phosphatase and Tensin Homolog	PTEN	P60484-1	1d5r	A	1-403
Thiopurine S-methyltransferase	TPMT	P51580	2h11	A	1-245
Cytochrome P450 2C9	CYP2C9	P11712-1	1r9o	A	29-490
Nucleotide triphosphate diphosphatase	NUDT15	Q9NV35	5bon	A+B	1-164
Aspartoacylase	ASPA	P45381	2o53	A+B	1-313
E3 ubiquitin-protein ligase parkin	PRKN	O60260-1	5c1z	A	1-465

Table S1. Overview of structure and sequence data used for analysis. Protein sequences are given by their UniProt identifiers and crystal structure input files (***Lee et al., 1999***; ***Wu et al., 2007***; ***Wester et al., 2004***; ***Carter et al., 2015***; ***Le Coq et al., 2008***; ***Kumar et al., 2015***) by their PDB identifiers. We used the PDB file chains and residues noted in the last two columns.

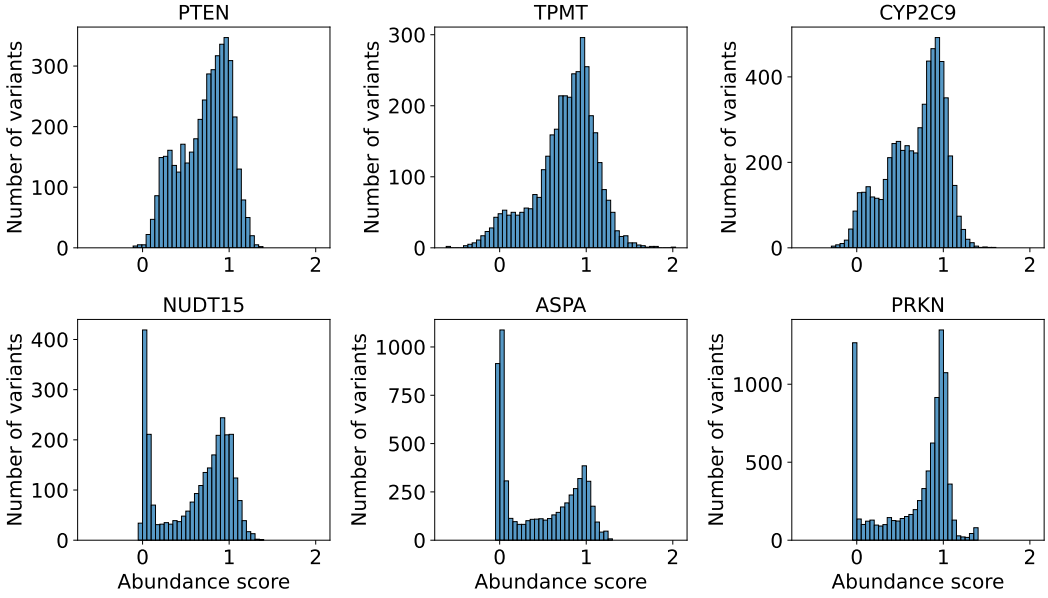

Figure S1. VAMP-seq abundance score distributions shown separately for each of the six datasets included in our analysis. The datasets only include scores for single residue substitution variants at residue sites in soluble protein regions.

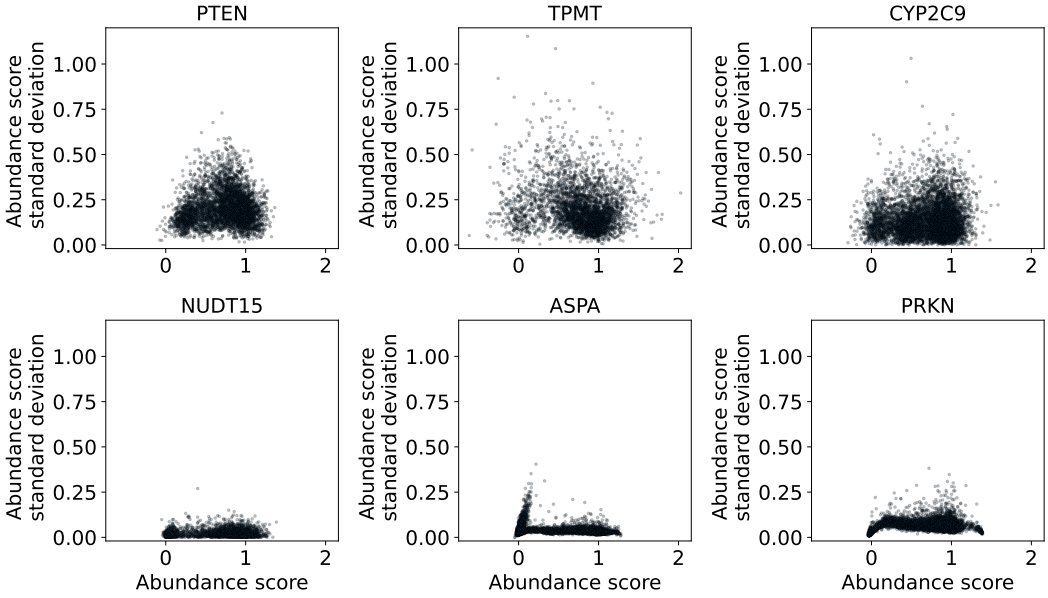

Figure S2. VAMP-seq abundance score standard deviations plotted as function of abundance scores separately for each VAMP-seq dataset. The standard deviations were calculated using a varying number of experimental replicates in the original VAMP-seq publications.

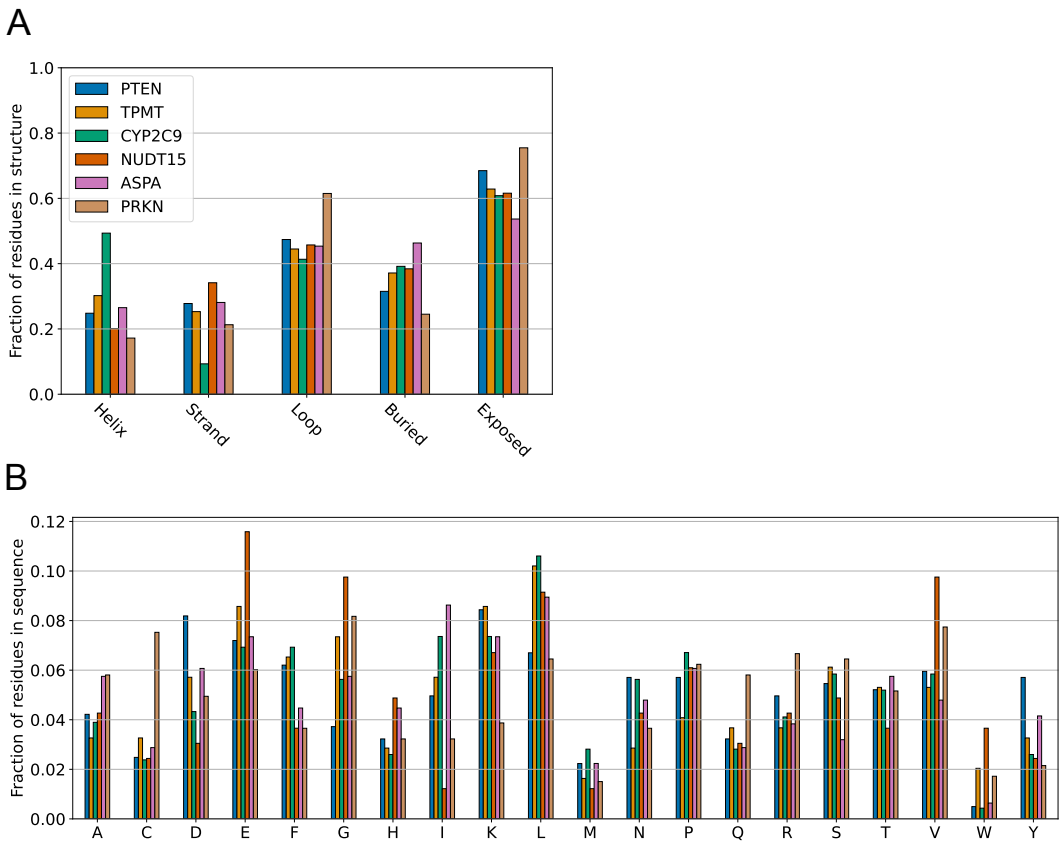

Figure S3. Summary of protein structure and sequence compositions. (A) The per protein fractions of residues forming different types of secondary structure are shown alongside with the fractions of residues found at structurally buried and solvent-exposed sites. For NUDT15 and ASPA, fractions were calculated using homodimer structures. The six proteins have relatively similar structural compositions, however with exceptions such as the relative helical enrichment in CYP2C9 and the loop and thereby also exposed site enrichment in PRKN. (B) Protein sequence compositions are similarly shown as residue type fractions with respect to the total number of residues in each protein.

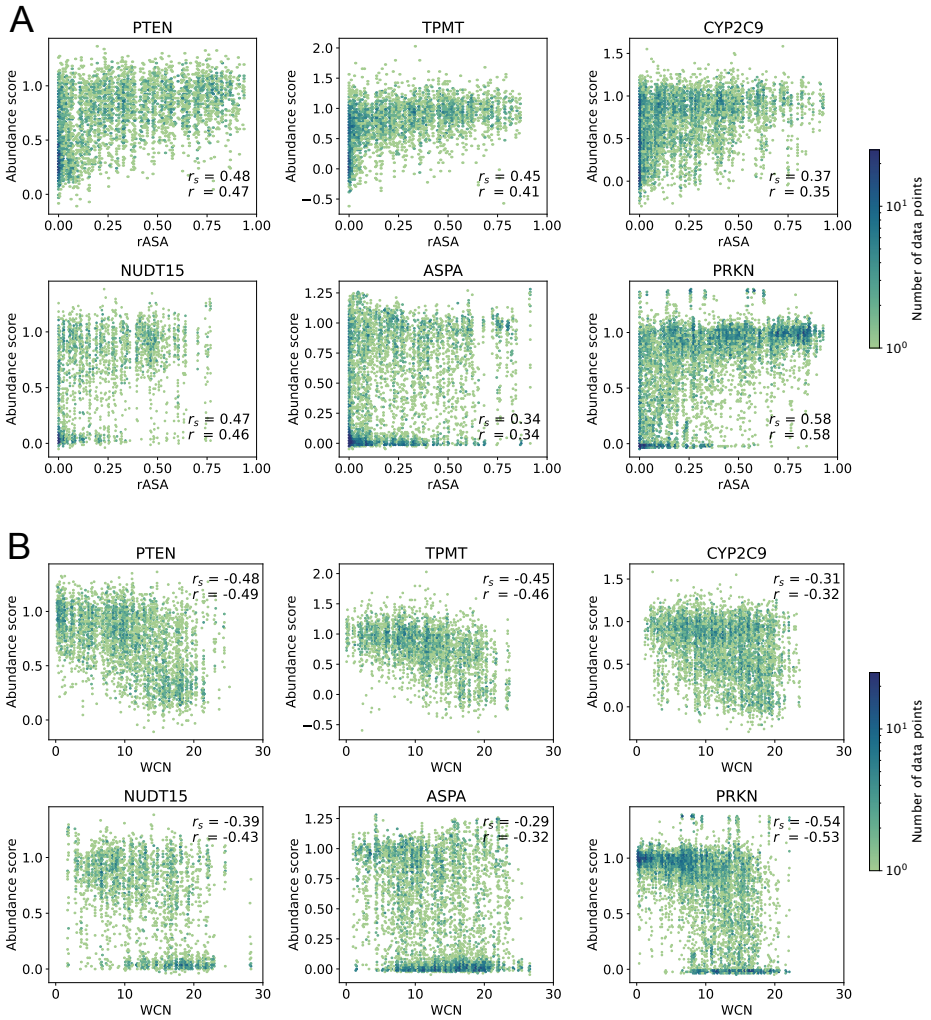

Figure S4. rASA and WCN correlate with single residue substitution abundance scores. Abundance scores for all single residue substitution variants are plotted against residue (A) rASA and (B) WCN values calculated using the wild-type protein structures. Pearson's correlation coefficient r and Spearman's rank correlation coefficient r_s between abundance scores and rASA or WCN values were calculated for each protein and are shown in the indvidual plots.

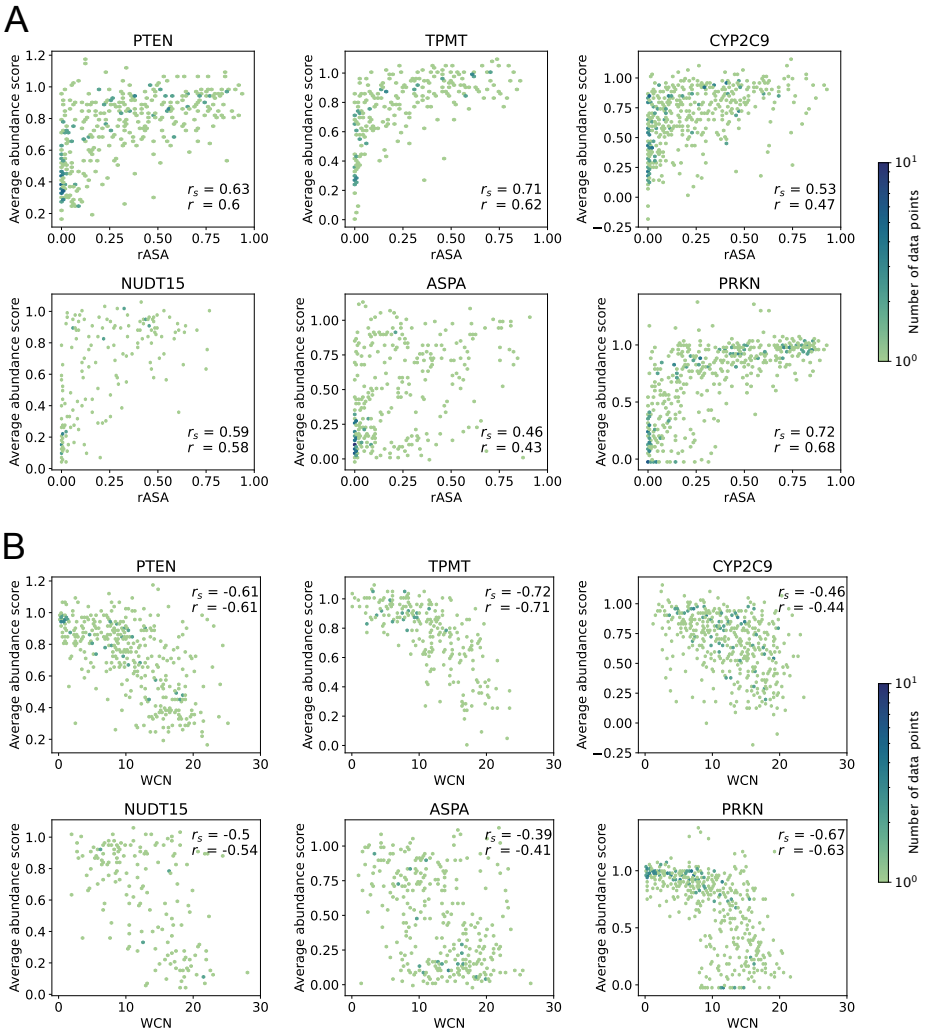

Figure S5. rASA and WCN correlate with residue-averaged abundance scores. Residue-averaged abundance scores are plotted against residue (A) rASA and (B) WCN values calculated using the wild-type protein structures. Pearson's correlation coefficient r and Spearman's rank correlation coefficient r_s between residue-averaged abundance scores and rASA or WCN were calculated for each protein and are shown in the individual plots. Averages are shown for all residues with abundance scores available, even if only one or few abundance scores have been reported for a given residue.

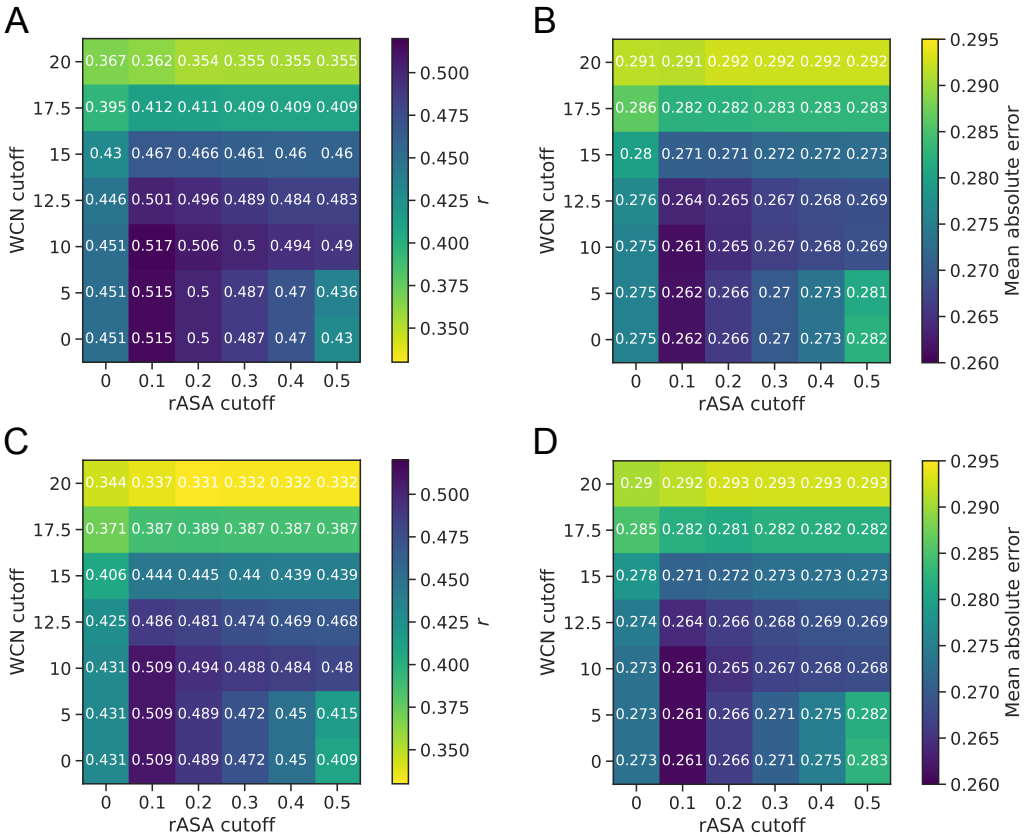

Figure S6. Grid search for selection of structure feature cutoffs to classify residues as solvent-exposed or structurally buried. (A) Pearson's correlation coefficient r between experimental and predicted abundance scores, with predictions based on exposure-based substitution matrices of average abundance scores calculated using different rASA and WCN cutoff values to classify residues as buried or exposed. Predictions were made using leave-one-protein-out cross-validation, and r is an average of results obtained for each of the proteins in our analysis. (B) Mean absolute error between between experimental and predicted abundance scores for the same predictions that results are shown for in panel A. Based on the results shown in panels A and B, we have used an rASA cutoff value of 0.1 to classify residues as solvent-exposed or buried in all other analyses in this work. (C,D) Results for grid search analysis similar to the analysis presented in panel A and B, but using median rather than average abundance scores to construct substitution matrices. We explored if using exposure-based substitution matrices of median abundance scores rather than average abundance scores would result in higher prediction accuracy. We found that, for our selected cutoffs, both the r and the MAE between experimental and predicted abundance scores are highly similar for the median- and average-based matrices.

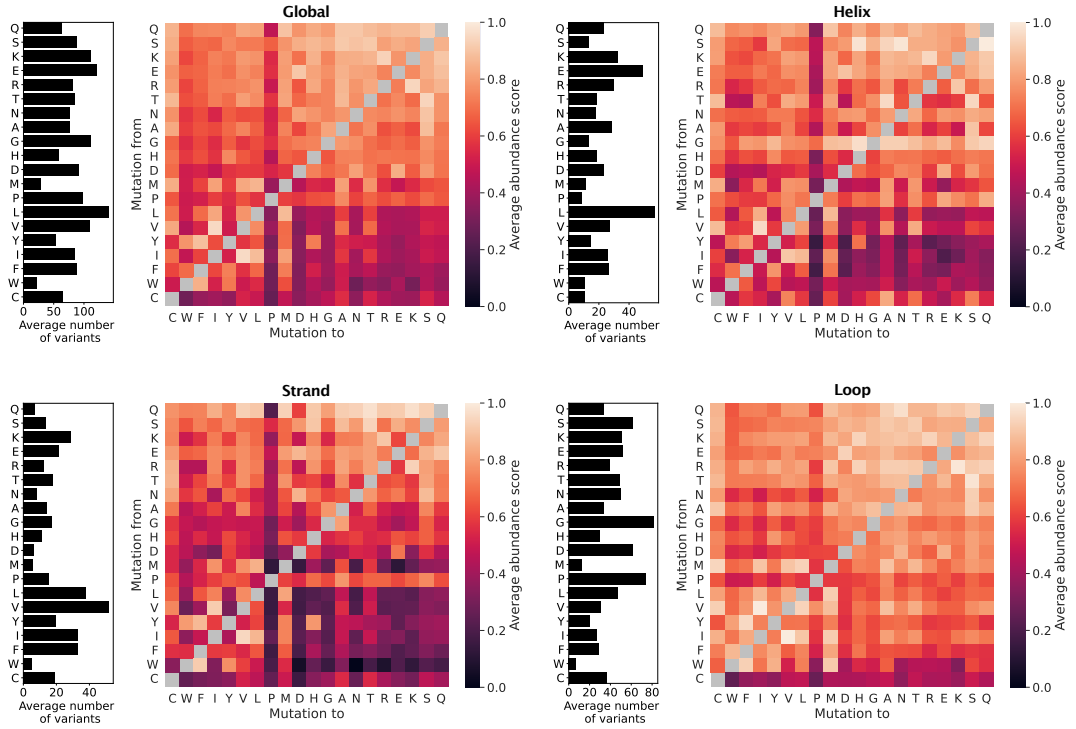

Figure S7. Average abundance score substitution matrices calculated using the six VAMP-seq datasets. The average score matrices were calculated by averaging over all scores, scores for residues forming helix, scores for residues forming strand and scores for residues forming loop structure, with structural context evaluated on wild-type structures. In each panel, the bar plot to the left of the average score matrix shows the average number of data points used to calculate the averages in a matrix row.

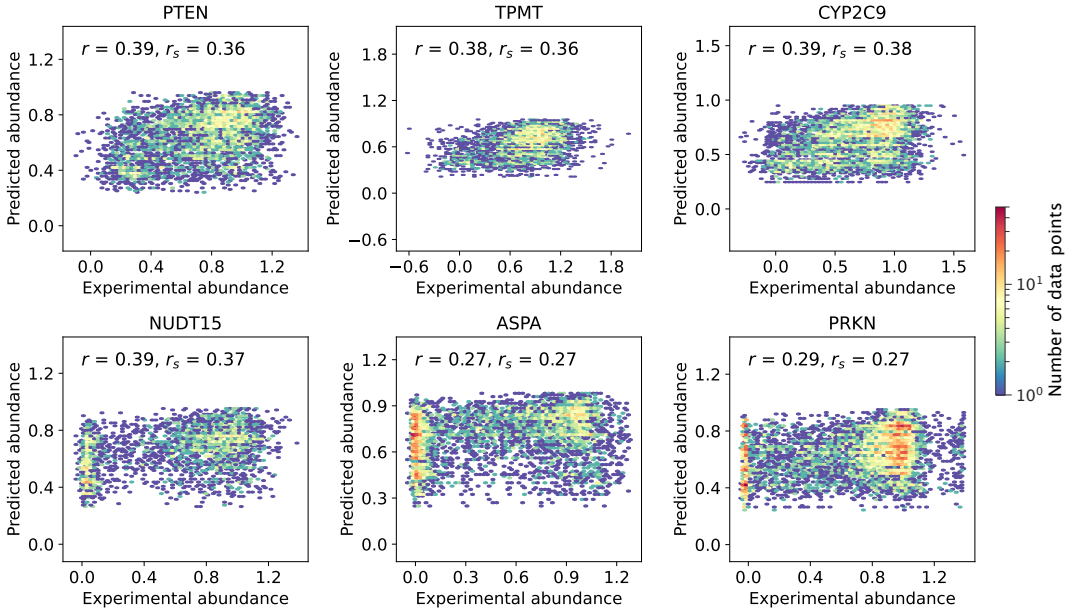

Figure S8. VAMP-seq abundance scores plotted against abundance score predictions obtained from average abundance score substitution matrices constructed without consideration of the structural context of the wild-type residue (Global in Fig. 2). All predictions were performed using using leave-out-one-protein cross-validation. Data point density is shown using an upper limit of 50 on the colour scale, meaning that a bin will be coloured red if it contains 50 data points or more.

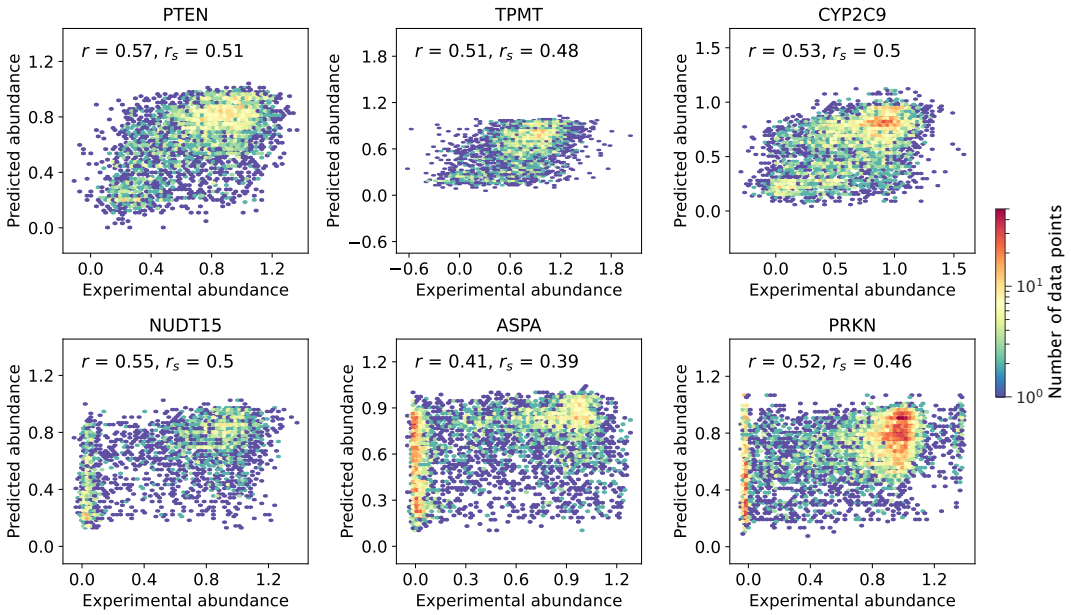

Figure S9. VAMP-seq abundance scores plotted against abundance score predictions obtained from average abundance score substitution matrices constructed by considering the degree of solvent-exposure of the wild-type residue (Exposure in Fig. 2). All predictions were performed using using leave-out-one-protein cross-validation. Data point density is shown using an upper limit of 50 on the colour scale, meaning that a bin will be coloured red if it contains 50 data points or more.

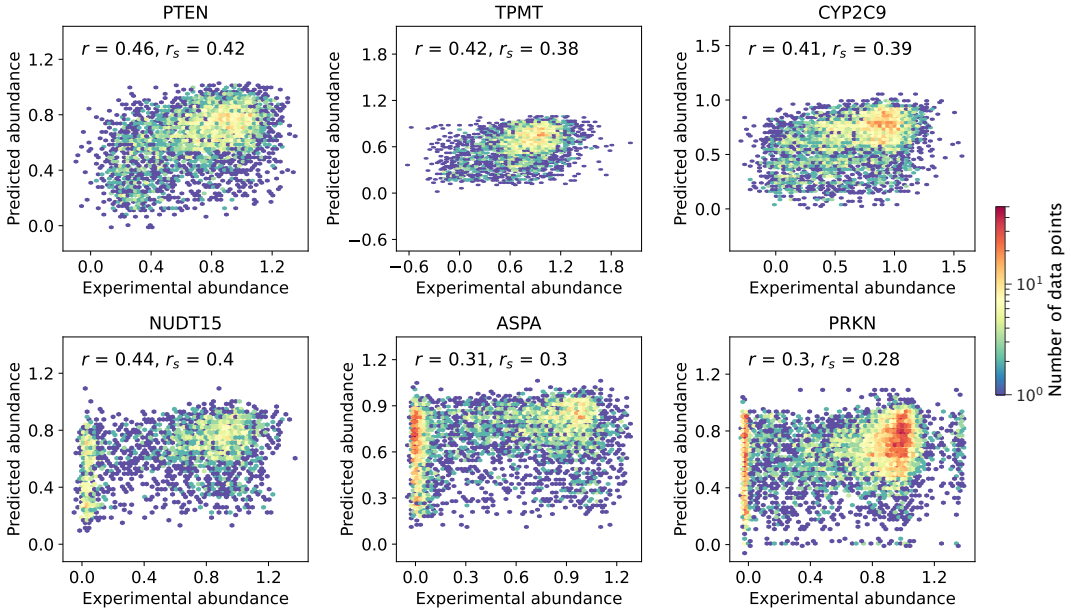

Figure S10. VAMP-seq abundance scores plotted against abundance score predictions obtained from average abundance score substitution matrices constructed by considering the secondary structure context of the wild-type residue (Secondary in Fig. 2). All predictions were performed using using leave-out-one-protein cross-validation. Data point density is shown using an upper limit of 50 on the colour scale, meaning that a bin will be coloured red if it contains 50 data points or more.

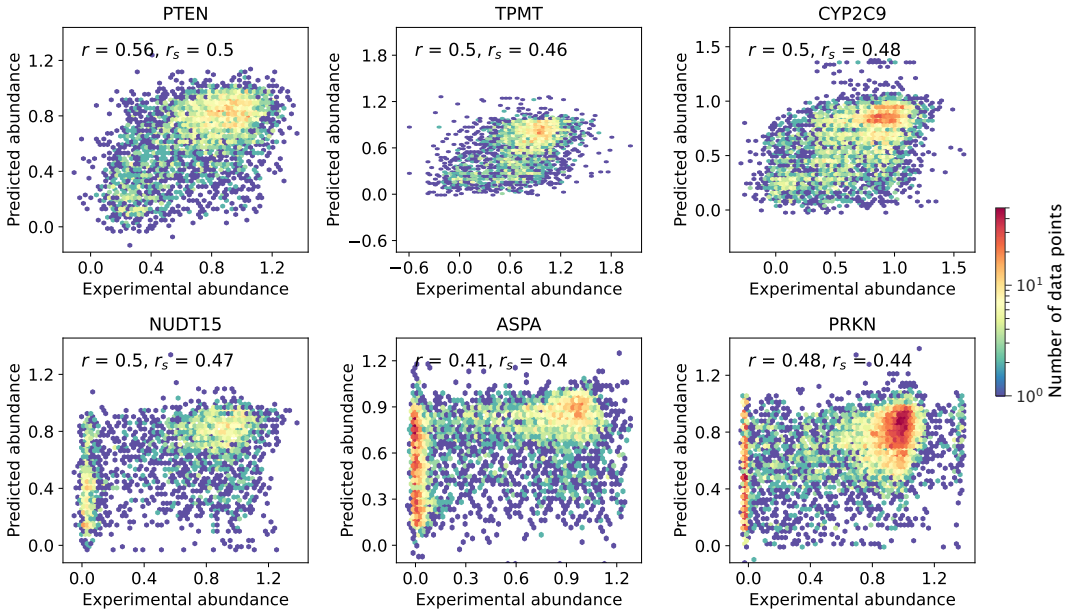

Figure S11. VAMP-seq abundance scores plotted against abundance score predictions obtained from average abundance score substitution matrices constructed by considering both the degree of solvent-exposure and the secondary structure context of the wild-type residue (Combined in Fig. 2). All predictions were performed using using leave-out-one-protein cross-validation. Data point density is shown using an upper limit of 50 on the colour scale, meaning that a bin will be coloured red if it contains 50 data points or more.

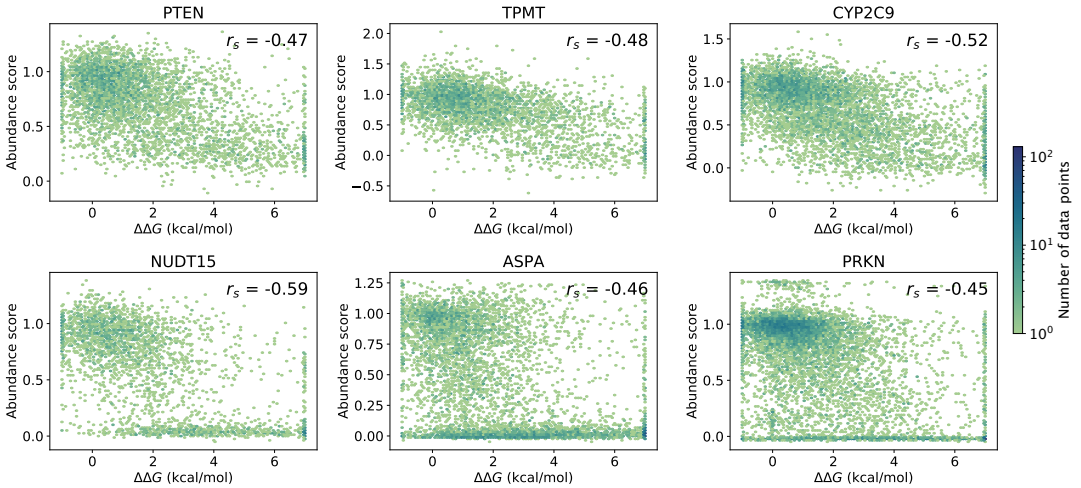

Figure S12. Variant abundance scores correlate with calculated ΔΔG values. The ΔΔG for all single residue substitution variants in each of the six proteins was estimated using Rosetta and correlate moderately well with variant abundance scores, as indicated with the r_s value per dataset in the individual plots. Data point density is shown using an upper limit of 130 on the colour scale.

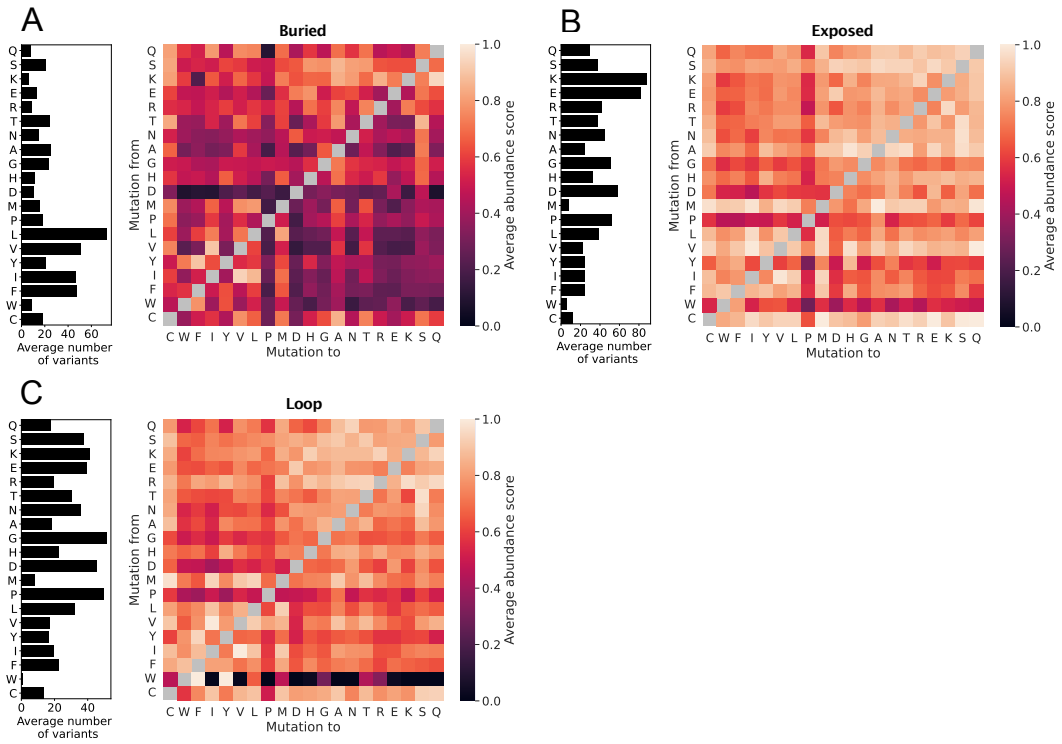

Figure S13. Average abundance score substitution matrices for (A) buried, (B) exposed and (C) loop environments calculated without abundance scores from the PRKN VAMP-seq dataset, but including all data from the five remaining datasets.

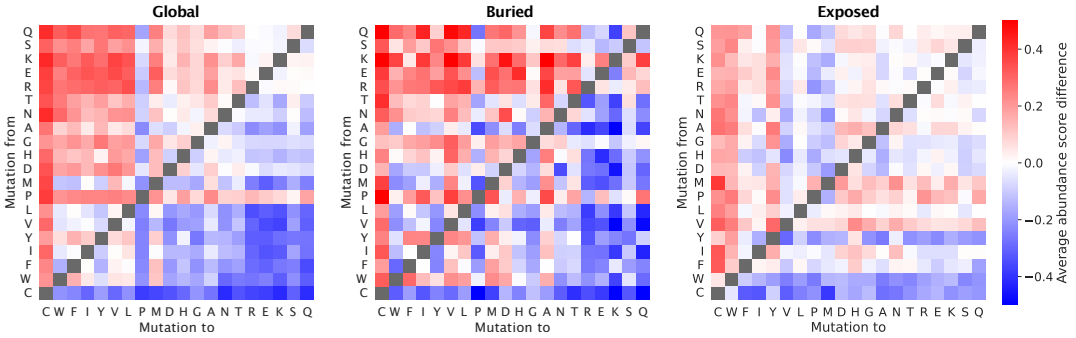

Figure S14. Heatmaps indicating the degree of symmetry across the diagonal in average abundance score substitution matrices. The symmetry was for each of the three residue environments (global, buried and exposed) evaluated for a given substitution type by subtracting the average abundance score for the reverse substitution from the average abundance score of the forward substitution. Hence, white indicates that a given residue pair behaves symmetrically, red indicates that the substitution is less disruptive in the forward than in the reverse direction, and blue means that the substitution is more disruptive in the forward than in the reverse direction.

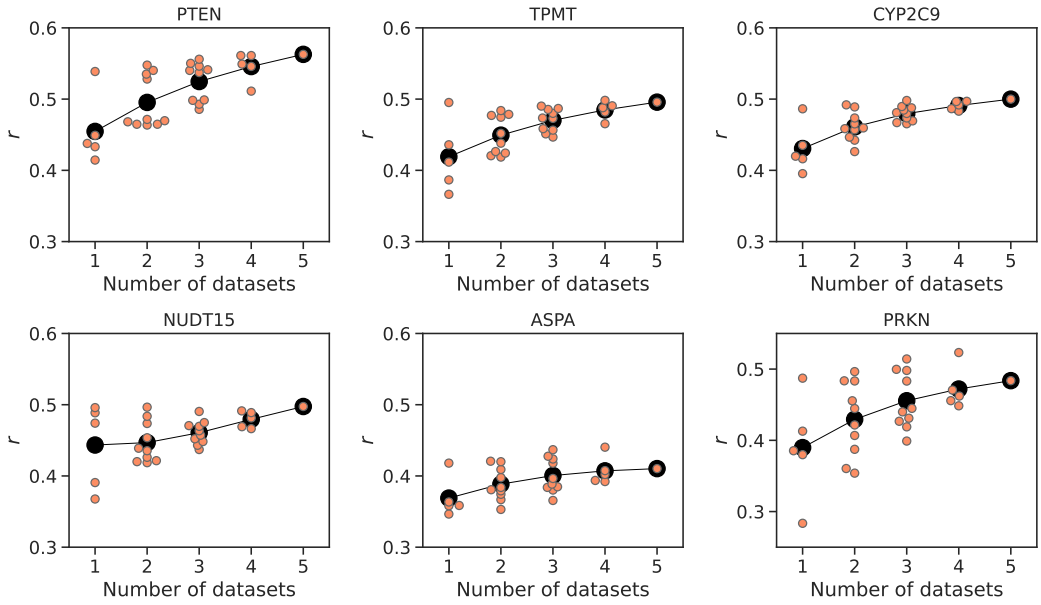

Figure S15. Correlations between experimental abundance scores and abundance scores predicted from the six average abundance score substitution matrices that consider both residue burial and secondary structure context of the wild-type residue. Scores were predicted for each protein (plot title) using average abundance score substitution matrices calculated with an increasing number of VAMP-seq datasets, though always leaving out the dataset for which predictions are performed. Orange data points mark prediction results from a single specific combination of datasets, and black data points are the average of the orange ones.

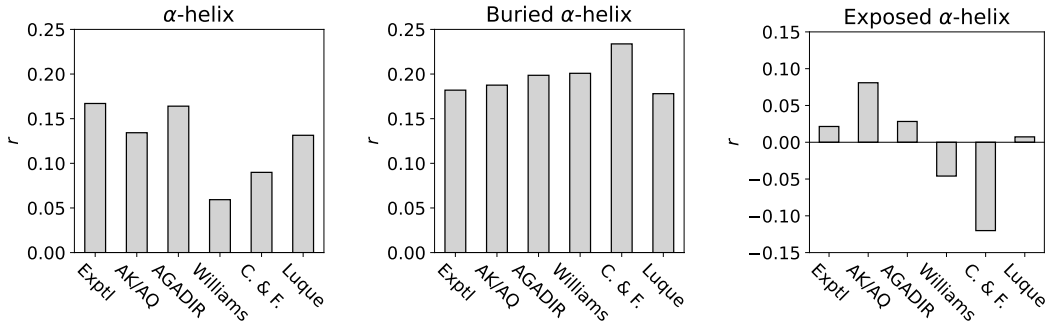

Figure S16. Analysis of the impact of amino acid helix propensity on average abundance scores. Pearson's correlation coefficient, r, between the average abundance scores for residues sitting in α-helical structure (either all α-helical structure or in only buried or exposed α-helical structure) and substitution matrices constructed from different helix propensity scales reporting on the $\Delta\Delta G$ of helix residue substitutions. Helix propensity scales were obtained from and are named as in previous work comparing the different scales (***Pace and Scholtz, 1998***). Explt scale reports on helix propensities for solvent-exposed, non-capping residues (***Pace and Scholtz, 1998***), AK/AQ (***Rohl et al., 1996***) and AGADIR (***Muñoz and Serrano, 1995***) were constructed from experimental data on peptides in solution, and C. & F. (***Chou and Fasman, 1978***) and Williams (***Williams et al., 1987***) scales are based on the frequency of amino acid occurrence in α-helices, buried as well as exposed. Finally, the Luque scale was originally derived from structure-based thermodynamical calculations and reports on helix formation propensities for residues in solvent-exposed helices (***Luque et al., 1996***).

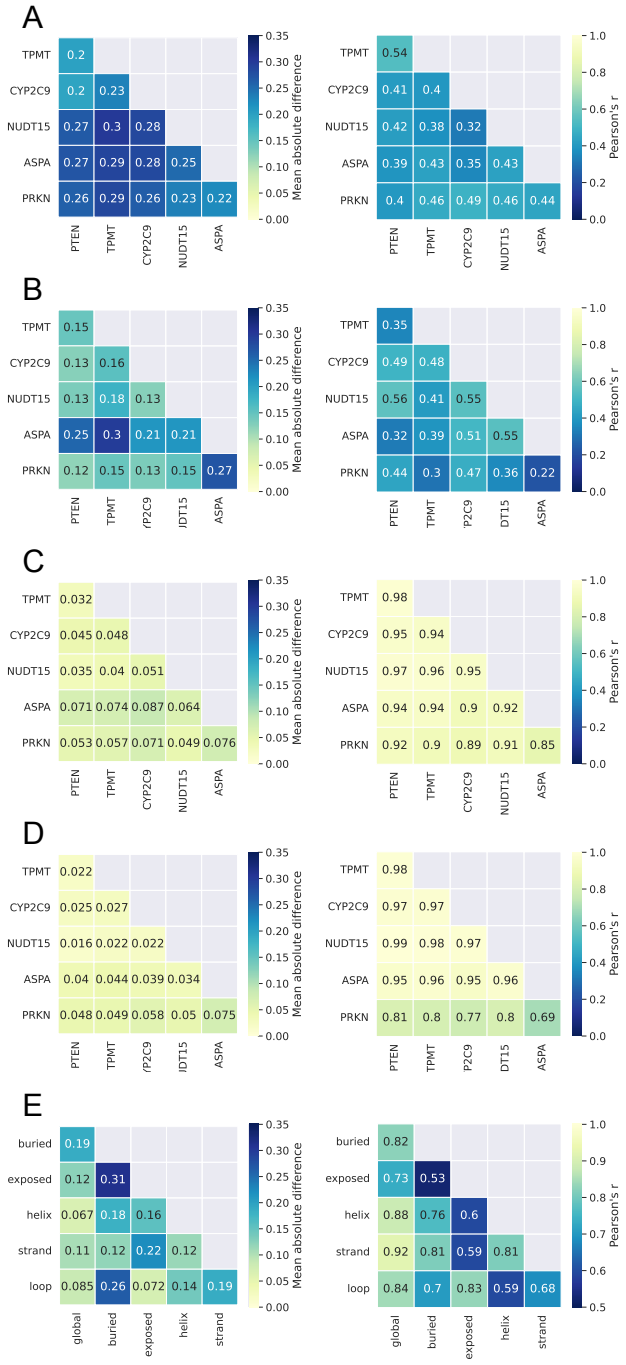

Figure S17. Comparison of average abundance score substitution matrices across proteins and residue environments. The mean absolute error and correlation coefficient were calculated between pairs of substitution matrices considering all abundance score averages in the two matrices to evaluate matrix similarity. (A) Comparison of buried environment matrices that were each calculated using data from only a single protein. Protein names on the axes thus indicate the single dataset used for the substitution matrix calculation. (B) Comparison of exposed environment matrices each calculated with data from single a protein. (C) Comparison of buried environment matrices, with matrices calculated using five out of six VAMP-seq datasets. Protein names on the axes indicate which dataset was omitted from the substitution matrix calculation. (D) Comparing matrices for exposed environments, with matrices calculated using five out of six VAMP-seq datasets. (E) Comparing matrices for different structural environments using matrices based on all data from all six proteins.

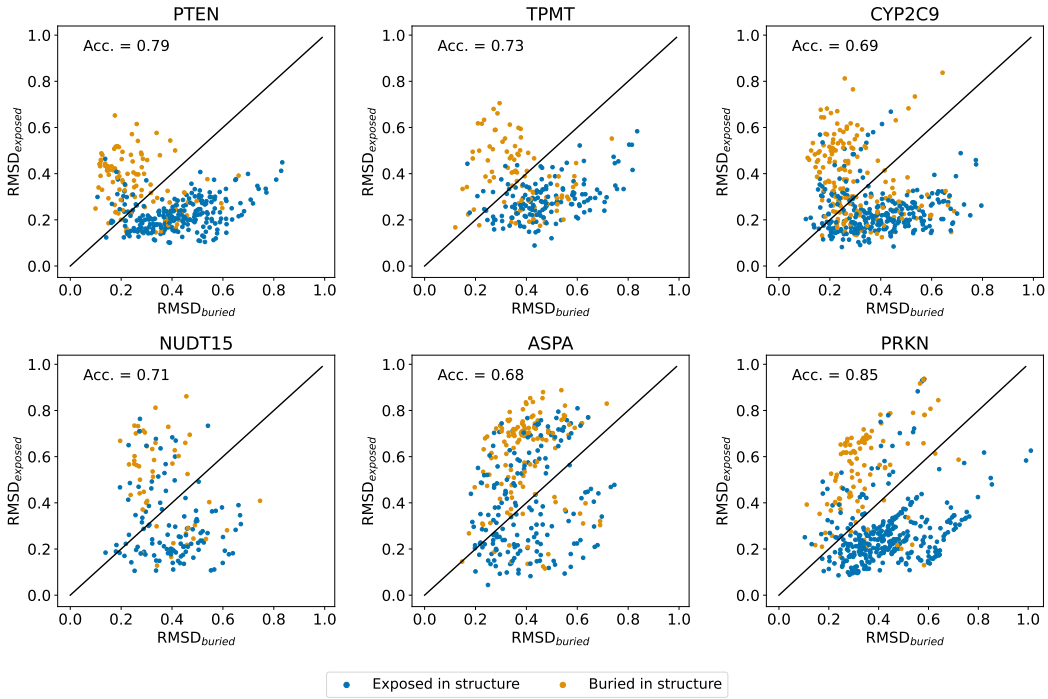

Figure S18. Discovering residues with abundance score substitution profiles non-typical for their structural environment. Each datapoint in the plots corresponds to a single residue coloured by its wild-type structure environment type and for which we calculated $RMSD_{exposed}$ and $RMSD_{buried}$. Solvent-exposed residues (blue) are expected to have $RMSD_{exposed} < RMSD_{buried}$ and thus appear below the plot diagonals, while the opposite is true for buried residues (yellow). Blue datapoints falling above the diagonal thus correspond to solvent-exposed residues with substitution profiles most similar to the average profile of buried residue, and yellow datapoints below the diagonal represent buried residues with substitution profiles relatively similar to the average profile of exposed residues. We quantified the extent to which buried and exposed residues respectively satisfy $RMSD_{buried} < RMSD_{exposed}$ and $RMSD_{exposed} < RMSD_{buried}$ by calculating the balanced classification accuracy (Acc.) per dataset. Data is only shown for residues with a least five measured abundance scores.

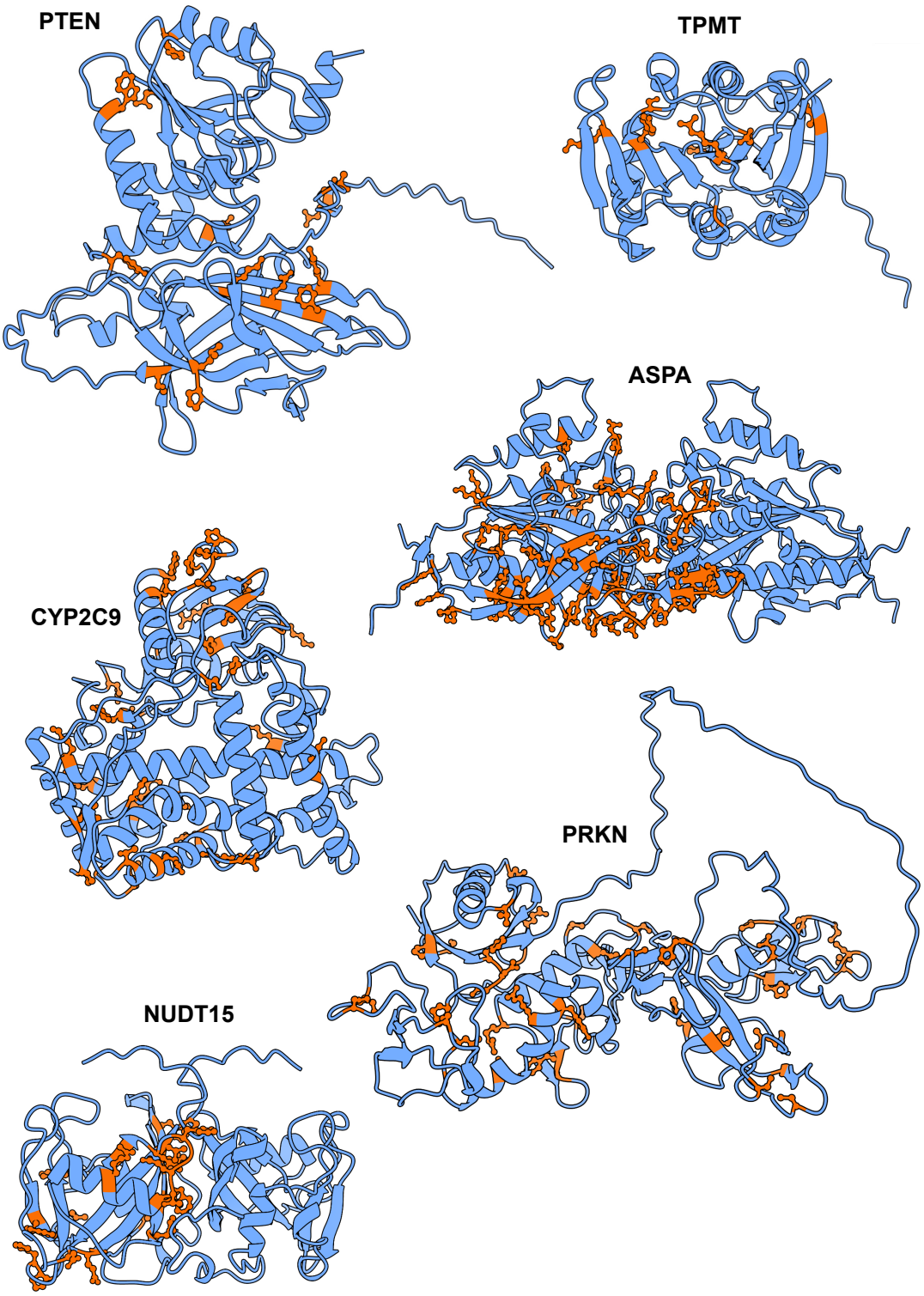

Figure S19. Protein structures with solvent-exposed residues found to have a smaller $RMSD_{buried}$ than $RMSD_{exposed}$ shown in dark orange. To make the results easier to interpret visually, only residues with a difference between $RMSD_{exposed}$ and $RMSD_{buried}$ larger than 0.05 are coloured orange here. NUDT15 and ASPA are shown as homodimers, but the exposed residues discovered in the analysis are shown for only one of the monomers in the complexes.